Four-Point Bending Testing of 8-in. (200-mm) Diameter AWWA C900 DR14 iPVC Pipe with ReiberLok

Shih-Hung Chiu

Gersena Banushi

Shakhzod Takhirov

Kenichi Soga

CSI Report 2026/01
Center for Smart Infrastructure (CSI)
Department of Civil and Environmental Engineering
University of California, Berkeley May 2026

EXECUTIVE SUMMARY

This report describes the experimental results of a four-point bending testing of 8 inch AWWA C900 DR14 iPVC pipes with a joint fitting. The pipe is corrosive resistant and is known to be capable of tolerating large deformations to improve seismic resiliency. The ReberLok gasket is used for connecting the pipes for this experiment. The lab test was conducted under a monotonic force applied at the center of the specimens perpendicular to the pipeline direction. It was tested up to severe pipe damage or significant water leakage. Failures in both the pipe and fitting initiated near the ReiberLok gasket, driven by local stress concentrations. Distributed fiber optic sensors were used to capture pipeline behavior, providing insight into deformation and failure mechanisms. Axial strain measurements reveal that the strain patterns generally adhered to the bending theorem. Compressive strains were observed on the top side, tensile strains on the bottom, and minimal strains on the springlines. Hoop strain analysis showed circumferential strain behavior opposing the axial strains, consistent with Poisson's effect. Expansion on the bottom side of the fitting was observed, attributed to the rotation of the pipe within the fitting. Detailed 3D finite element models were constructed and calibrated with the experimental data, aiming to better understand the pipeline behavior considering its complex material nonlinearities and contact interaction of the pipe-joint components.

Keywords: ***iPVC pipe, water pipelines, fiber optic, leakage, sensors, finite element.***

ACKNOWLEDGMENTS

The funding for this project was provided by the East Bay Municipal Utility District (EBMUD) and PPI Pipe. The completion of the work would not be possible without the support of John Kochan, Irik Larson, and Phillip Wong of the University of California, Berkeley. Active involvement and guidance from David Katzev of EBMUD and Agnes HyeJung Lee of PPI America, Inc. are greatly appreciated.

DISCLAIMER

CONTENTS

LIST OF FIGURES

LIST OF TABLES

1 Introduction

This report summarizes the experimental results of a four-point bending test performed on 8-inch AWWA C900 DR14 iPVC pipes with a joint fitting. The pipe is corrosive resistant and is known to be capable of tolerating large deformations which could improve the seismic resiliency of pipeline systems. Two identical pipes were joined together by inserting them into a fitting that passed through a circular rubber gasket with multiple teeth. The ReiborLok gasket was adopted in this experiment. The purpose of the rubber gasket is to prevent water from leaking, while the teeth are designed to bite into the connected pipe as a locking mechanism, thus restraining the pipes from moving apart. The fully assembled fitting and the cross section of the fitting are shown in Figure 1-1 and the ReiberLok gasket is shown in Figure 1-2.

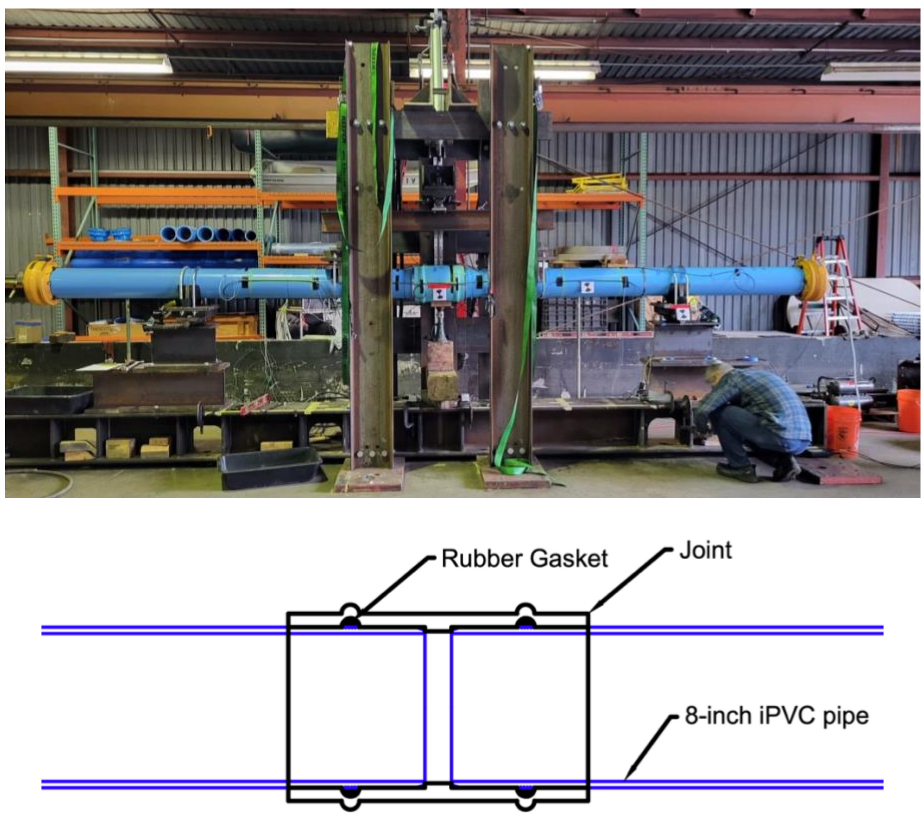

Figure 1-1 Schematic of the fitting of AWWA C900 DR14 iPVC pipe

Figure 1-2 Gaskets for the specimens

Distributed fiber optic sensors (DFOS) were employed to measure continuous strain development along the longitudinal and circumferential directions. Position transducers tracked specimen movement, load cells measured applied force, and pressure gauges monitored internal water pressure. Based on experimental data, the following sections provide detailed information about the modes and mechanisms of deformation and failure. Finite element analysis was performed to understand the pipeline behavior of the complex material nonlinearities and contact interaction of sleeve joint and pipes under bending condition.

2 Experimental Setup

The experimental setup was designed as a self-reacting system, as shown in Figure 2-1. The load was applied by a 20-kip hydraulic actuator with a stroke of ± 40 inches. The actuator's rod was guided by a linear bearing system to keep the direction of the loading vertical. Saddles were used at two reaction points to distribute the force evenly and to avoid localized failures of the pipe. These saddles were free to rotate and slide in the horizontal plane because the rollers are installed under the saddles. The distance between the reaction rollers was 150 inches at the beginning of the test. A similar approach was utilized for the two loading points on top of the pipe. The force from the actuator was transferred to the pipe via a wide flange I-beam. The load was applied at the mid-span of the I-beam. A special clevis system was introduced at this location to allow the I-beam's rotations to ensure that the actuator force is evenly transferred to two loading points. The saddles with the rollers were also used at these locations. The initial distance between the loading points was 60 inches. The rollers were set free to slide. A few safety measures were introduced to keep the hardware together in case of unexpectedly large sliding occurs.

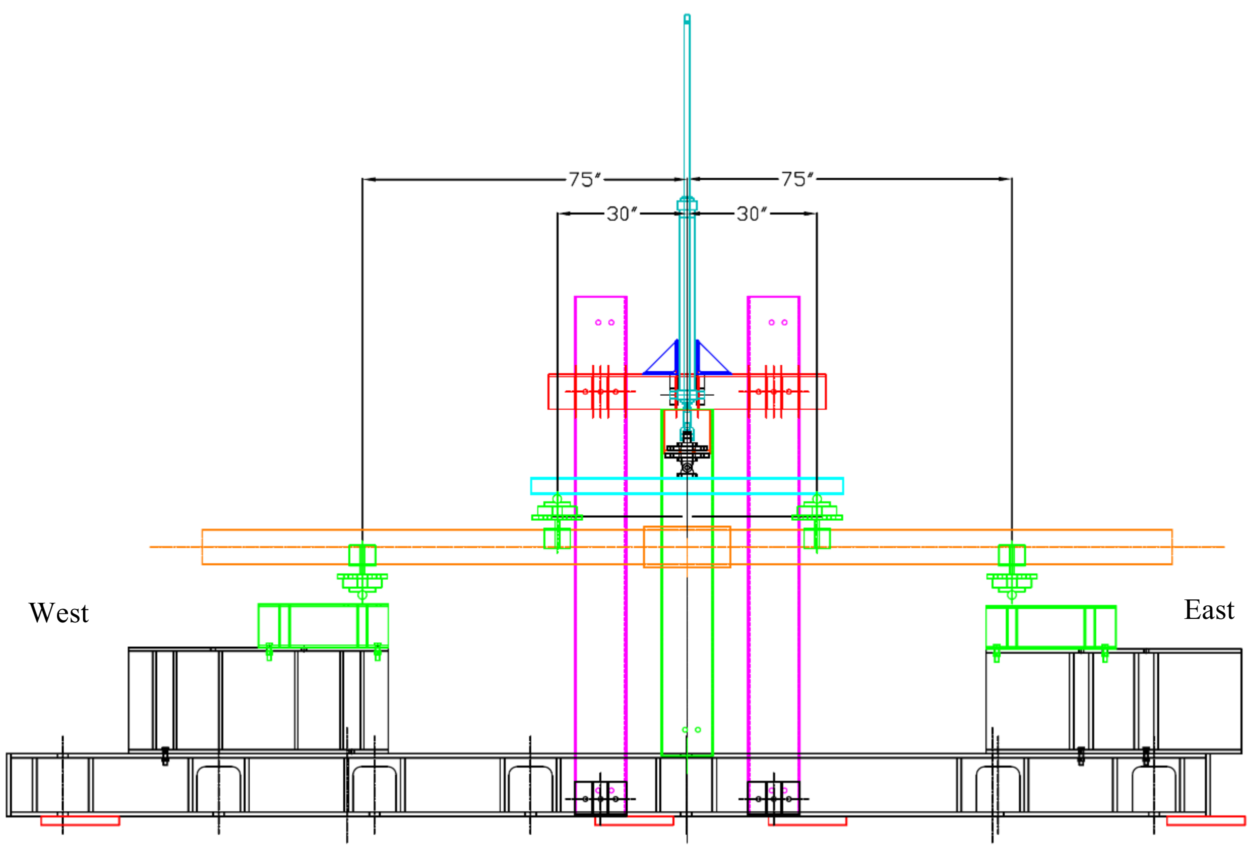

Figure 2-1 Schematic drawing of the experimental setup

As shown in Figure 2-2, endcaps closed the pipe on both ends. One endcap received a water supply hose, whereas the other received an air bleeder hose. A pressure sensor was installed on the latter endcap to monitor the pressure inside the pipe. Prior to the test, the pipe was pressurized with water at 70 psi. A photo showing the experimental setup and the pipe during the test is given in Figure 2-3.

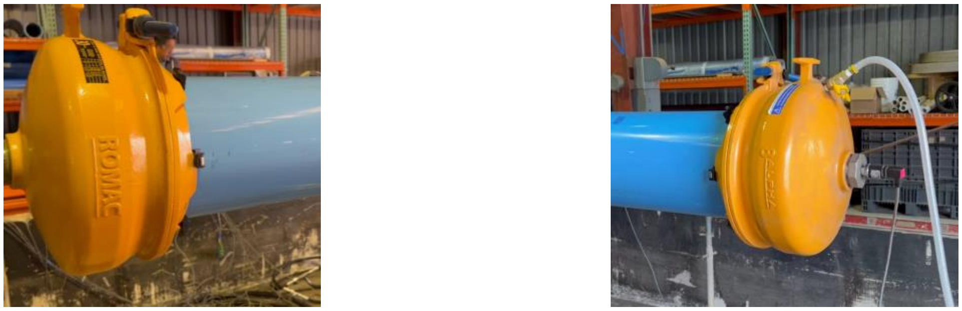

(a) Endcap on left side **(b) Endcap on right side**

Figure 2-2 Endcaps to enable water pressurization

Figure 2-3 Photo of the pipe during the test

A single pipe assembly was tested in the four-point testing configuration. The rubber gasket manufactured by Reiberlok was used inside the sleeve. The test runs are summarized in Table 2-1 Summary of test runs.

Table 2-1 Summary of test runs

No	Specimen name	Description	Date	Data files
1	CSI-2023-PPI-4PB01	Pressurization	03/26/2024	Run000
1	CSI-2023-PPI-4PB01	Bringing the loading beam into contact with the pipe	03/27/2024	Run001
2	CSI-2023-PPI-4PB01	Testing	03/27/2024	Run002

3 Instrumentation

The instrumentation consisted of conventional sensors (position transducer, load cell, pressure gage) and distributed fiber optic sensors. The instrumentation plan is discussed in the following sections.

3.1 Conventional Instruments

The experimental setup and the specimen were extensively instrumented. The instrumentation consisted of a load cell incorporated into the actuator, a water pressure gage, position transducers measuring the displacement of the pipes across the joint, and a position transducer monitoring the displacement of the sleeve on the loading side, as summarized in Table 3-1. In addition, fiber optic sensor was utilized, which will be discussed in the respective section.

Table 3-1 Summary of conventional instrumentation

Column No in data file	Channel name	Description	Measurement, units
3	Pacific - 1 (0:0:0) cyl pos	Displacement	Actuator displacement, in
4	Pacific - 2 (0:0:1) lc	Load cell	Applied force, lbs
5	Pacific - 3 (0:0:2) wtr press	Pressure gage	Water pressure, psi
6	Pacific - 69 (0:8:4) wp12	Position transducer	Vertical displacement of the sleeve's east end
7	Pacific - 70 (0:8:5) wp11	Position transducer	Triangulated measurement of in-plane and out-of-plane displacements: east
9	Pacific - 72 (0:8:7) wp9	Position transducer	
8	Pacific - 71 (0:8:6) wp10	Position transducer	Relative displacement: pipe vs sleeve
10	Pacific - 73 (0:9:0) wp8	Position transducer	Not connected
11	Pacific - 74 (0:9:1) wp7	Position transducer	Triangulated measurement of in-plane and out-of-plane displacements: west
12	Pacific - 75 (0:9:2) wp6	Position transducer	
13	Pacific - 76 (0:9:3) wp5	Position transducer	Vertical displacement of the sleeve's west end
14	Pacific - 77 (0:9:4) wp4	Position transducer	Joint rotation
15	Pacific - 78 (0:9:5) wp3	Position transducer	Joint rotation
16	Pacific - 79 (0:9:6) wp2	Position transducer	Joint rotation
17	Pacific - 80 (0:9:7) wp1	Position transducer	Joint rotation

Figure 3-1 shows position transducers used for monitoring the rotation of the joint. A schematic drawing of the instrumentation locations is presented in Figure 3-2.

Figure 3-1 Position transducers for rotation monitoring of the joint

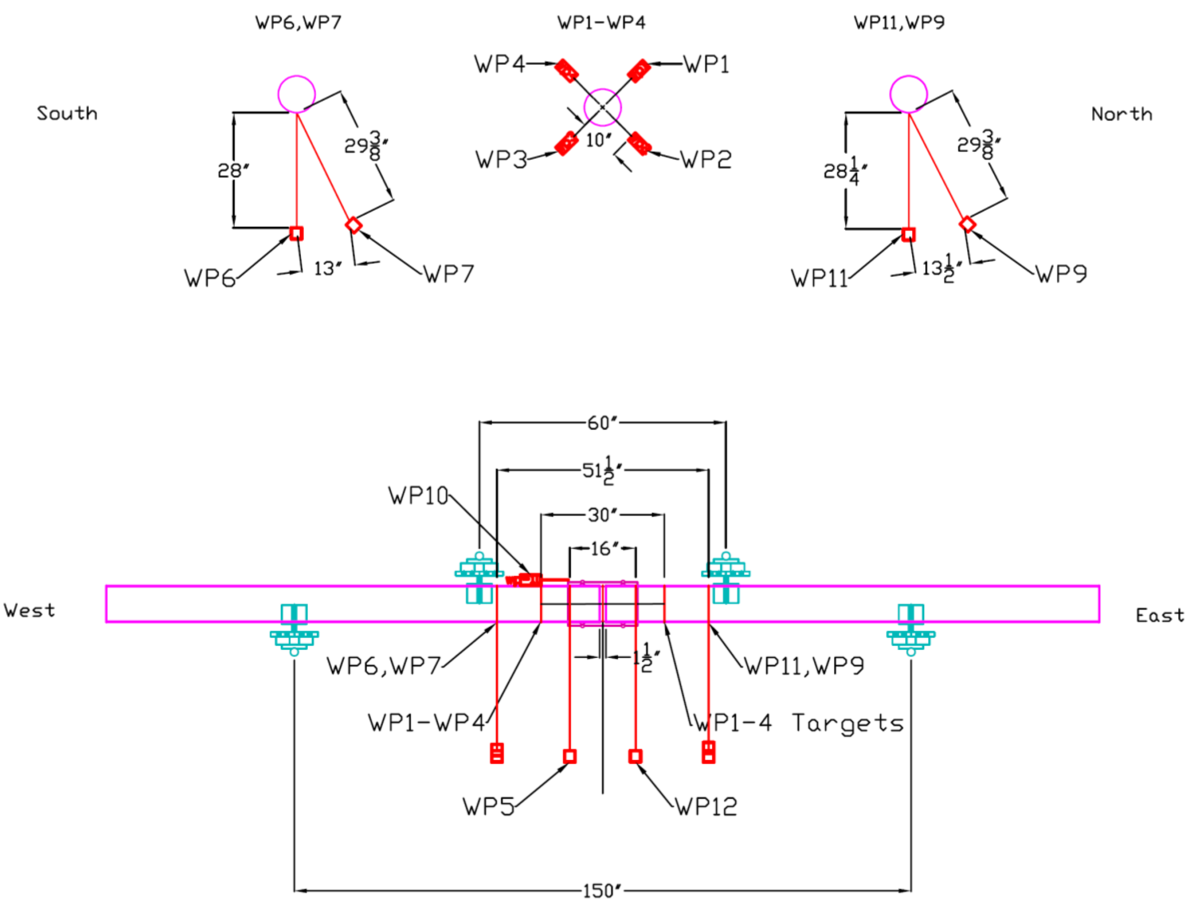

Figure 3-2 Position transducers for displacement monitoring of the pipe and the joint

3.2 Fiber Optic Sensors

Two types of fiber optic cables manufactured by NanZee Sensing Technology Co. were used; (a) 5 mm diameter armored cable (NanZee 5mm) and (b) 0.9 mm diameter cable (NanZee 0.9mm). Huntsman Araldite 2021-1 epoxy was used to attach the fiber optic cables to the pipes. Figure 3-3 shows the layout and locations of the sensors. NanZee 5mm cables (blue lines) were used in the longitudinal direction to mimic the use on construction sites. They were attached on both pipes, 90 degrees apart, named T, N, S, B. On the other hand, to better understand the deformation mechanism of the pipes, a thiner NanZee 0.9mm (red lines) was used for measuring circumferential strains, numbered S1-S10. Three circumferential sensors with about 18-inch spacing were installed on both pipes. In addition, two circumferential sensors were placed on both sides of each of the gaskets. Since there are two gaskets in the fitting to lock the two pipes, there are in total four circumferential sensors on the fitting. The local names of DFOS are listed in Table 3-2.

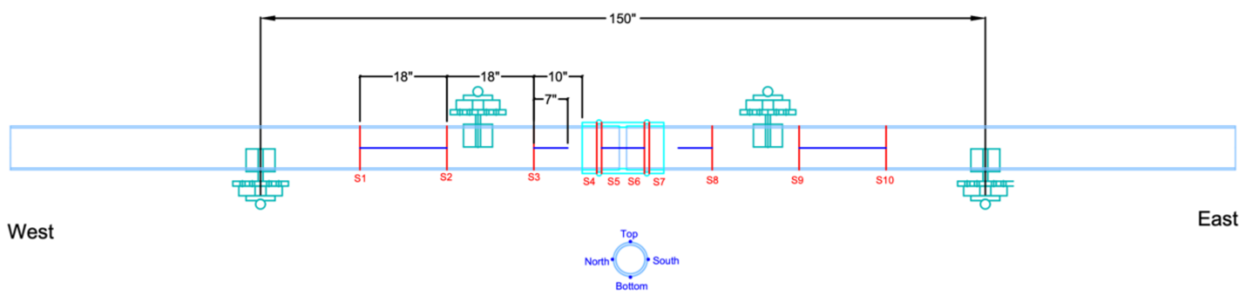

Figure 3-3 Instrumentation plan of fiber optic sensors of the specimens

Table 3-2 Summary of fiber optic sensors

Instrument	Location	Local Instrument Name
DFOS	54.375 inch west of center, Circumferential	S1
	36.375 inch west of center, Circumferential	S2
	18.375 inch west of center, Circumferential	S3
	5.375 inch west of center, Circumferential	S4
	4.375 inch west of center, Circumferential	S5
	4.375 inch east of center, Circumferential	S6
	5.375 inch east of center, Circumferential	S7
	18.375 inch east of center, Circumferential	S8
	36.375 inch east of center, Circumferential	S9
	54.375 inch east of center, Circumferential	S10
	Top, Longitudinal	T
	North, Longitudinal	N
	South, Longitudinal	S
	Bottom, Longitudinal	B

A Rayleigh-based optical frequency domain reflectometry (OFDR), Luna ODiSI 6100 series, was used in the experiments for data acquisition. The analyzer is capable of measuring up to 100 meters long fiber optic cable with an accuracy of less than ±1 micro strain when taking a measurement every 0.65mm. Appendix A provides more information about the cables and the analyzer.

4 Test Results

All test results are discussed in this section. In addition, a summary of the failure mode and performance of the 8 inch AWWA C900 DR14 iPVC pipes with ReiberLok gasket under four-point bending force is included.

4.1 Calculation Approach

The approach for calulating moment and two approaches for evaluating rotation are discussed herein. The system is considered to be a simple-supported beam. The self-weight, including the weights of the pipe and water, is assumed to be evenly distributed, and hence the moment introduced by self-weight is calculated based on equation (1), where w is the uniform load due to the self-weight, and l is the length of the pipe between the supports. The distance between the spports (l) is 150 inches. The additional moment applied to the central portion of the pipe is calculated using equation (2), where P is the actuator load, and L is the distance between the support and the loading location (i.e., 45 inches).

$$M_{distrib} = \frac{wl^2}{8} \tag{1}$$

$$M_{central} = \frac{PL}{2} \tag{2}$$

Regarding the roatation computation approach, the first method utilizes the measurements from vertical wire pots (VWPs). The pipes are assumed to be rigid bodies, and the rotations of the pipes are computed using equations (3) – (5). The vertical displacements of the pipes were measured by the VWPs that are located beneath the center (i.e., wp5, wp12) and the pipes (i.e., wp6 and wp11). θ_{bell} and θ_{spigot} are the rotations of the bell pipe and the spigot, respectively. The overall rotation, θ_{Total}, of the joint is defined as the sum of the two side angles.

$$\theta_{bell} = \tan^{-1}(\frac{wp5 - wp6}{distance\ between\ wp5\ \&\ wp6}) \tag{3}$$

$$\theta_{spigot} = \tan^{-1}\left(\frac{wp11 - wp12}{distance\ between\ wp11\ \&\ wp12}\right) \tag{4}$$

$$\theta_{Total} = \theta_{bell} + \theta_{spigot} \tag{5}$$

The second approach is based on the horizontal wire pots (HWPs) installed around the circumference of the bell. It is based on the fact that the virtical distance between the position transducers does not change. It assumes that the out-of-plane displacements are negligible. It is also assumed that the rotation of the pipe is the same on both sides of the joint. In this case:

$$\theta_{Total} = 2\tan^{-1}[0.5\frac{top\ disp. - bottom\ disp.}{distance\ between\ top\ \&\ bottom\ HWPs}] \tag{6}$$

where *top disp.* is the displacement measured by wp1 or wp4; the *bottom disp.* is the displacement measured by wp2 or wp3.

4.2 Moment and Rotation

The specimen was filled with water and pressurized to about 70 psi. Two testing stages were involved: (1) self-weight moving down, and (2) actuator pushing down. In the first stage, the temporary support were removed and the pipes were allowed to move downward due to their self-weight until reaching a static force equilibrium. Then, a monotonic force, perpendicular to the longitudinal axis of the pipeline, was applied at the center point of the load transfer beam. This force was then transferred to the pipes through the two loading saddles.

Figure 4-1 presents a schematic image showing the joint's deflection and rotation before and during the test. In addition, an actuator displacement is shown in the same image.

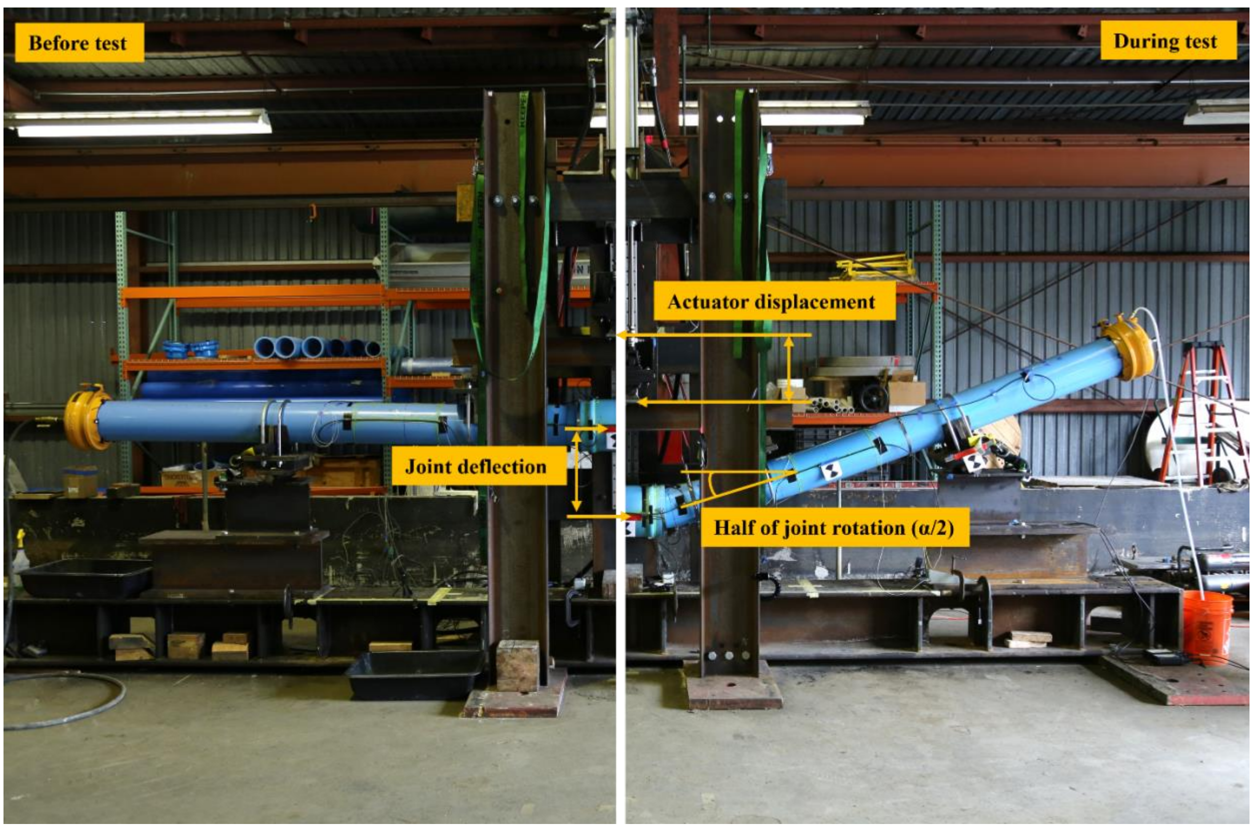

Figure 4-1 Schematic image explaining how the joint deflection and joint rotation are calculated

Figure 4-2 presents the load-joint deflection curves. The plot shows that the maximum actuator displacement was 15.21 inches, while the maximum joint deflection was approximately 19.73 inches. This outcome aligns with the similar triangle theorem, which predicts that the center of the pipe will move more than the displacement at the loading saddle location. Consequently, the joint deflection is larger than the actuator displacement.

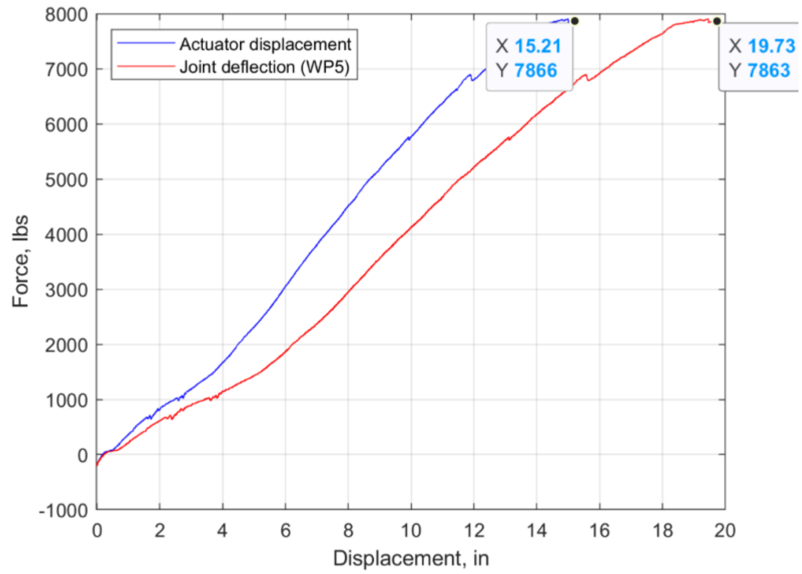

Figure 4-2 Force versus joint deflection and actuator displacement

The maximum joint rotation calculated from the two approaches are 1) 28.07 degree (VWP approach), and 2) 26.38 degree (HWP approach) with a maximum momet about 177.76 kip-in. The results from the two approaches align closely. The moment-rotation curves are shown in Figure 4-3 and the maximum values are given in Table 4-1.

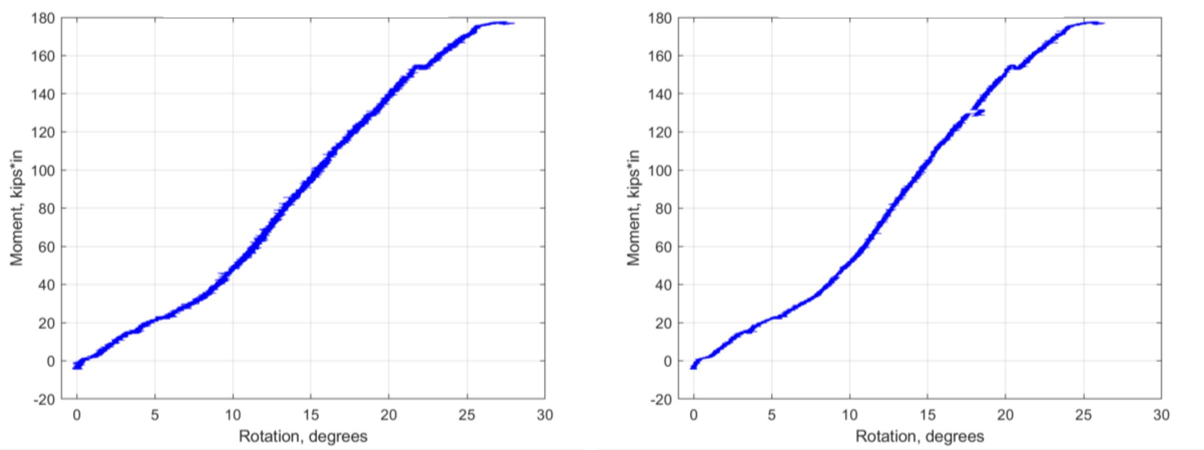

(a) **VWP approach**

(b) **HWP approach**

Figure 4-3 Rotation of the joint versus moment

Table 4-1 Summary of the tests

Max. Moment	Rotation – VWP approach	Rotation – HWP approach
177.76 Kip-in	28.07 degree	26.38 degree

4.3 Failure Mode

Figure 4-4 (a) gives a overall image of the specimen failure. It was observed on both the fitting and the west pipe, originating near the ReiberLok gasket. The gasket's small teeth, designed to grip the pipe and prevent separation, created local stress concentrations at these points. These stress concentrations initiated the failures, which then propagated from these locations.

The fitting failure began on the top side, where it experienced the highest compressive force, and propagated due to shear forces along the sides to the bottom, as shown in Figure 4-4(c). The west pipe then failed on the bottom side due to tensile stress. The initial crack on the pipe appeared beside the gasket, where high stress concentrations are anticipated. Shear crack propagating toward the top of the pipe, as shown in Figure 4-4(b).

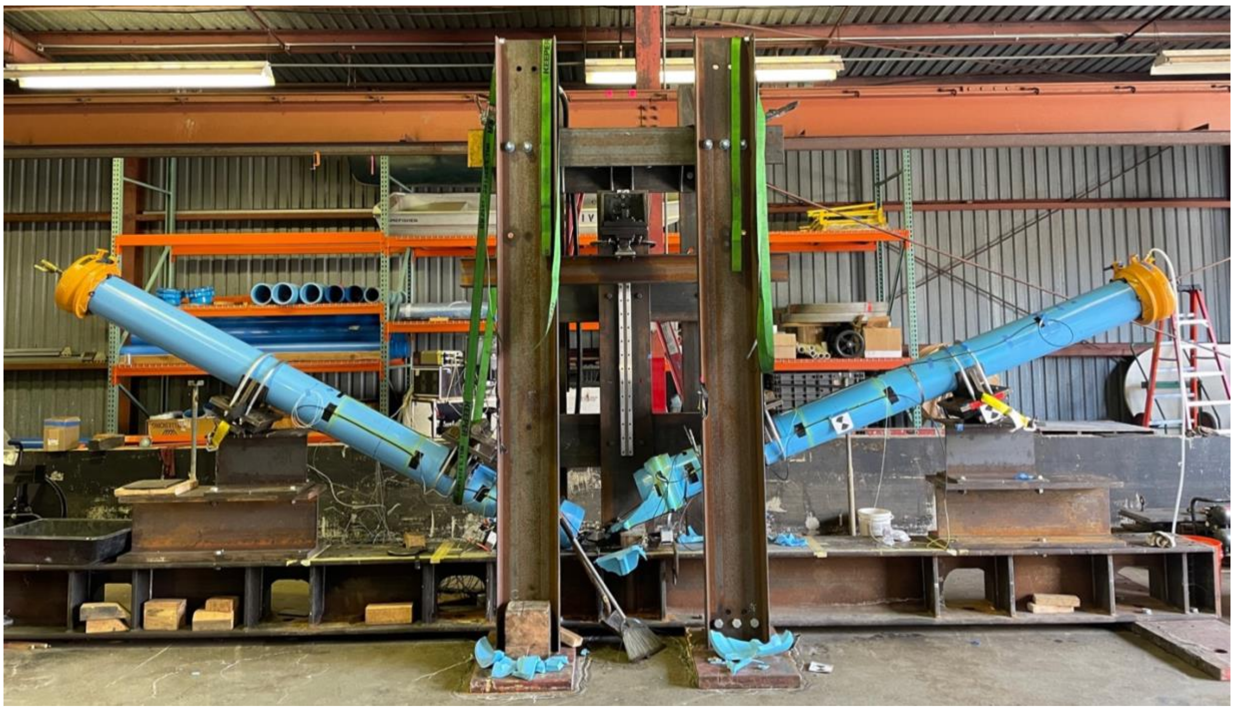

(a) Overall failure

(b) Failure on west pipe

(c) Failure on fitting

Figure 4-4 Failure of the specimen

4.4 Axial Strains

The axial strain results from the distributed fiber optic strain (DFOS) sensors are shown in Figure 4-5 and Figure 4-6. Figure 4-5 shows the relationship between the axial strain and axial loads at 3.5 inches east of S3 (west pipe) and 3.5 inches west of S8 (east pipe) (red squares in the figure), as measured by the longitudinal sensors. The strain development on both pipes follows the bending theorem, indicating compression on the top side, tension on the bottom side, and minimal stress on the sides. However, compressive strain is observed on the south side of the east pipe. This anomaly is attributed to the offset placement of the fiber optic sensors at this location. The sensor was positioned slightly towards the top side rather than perfectly on the springline, resulting in the observed compressive strain.

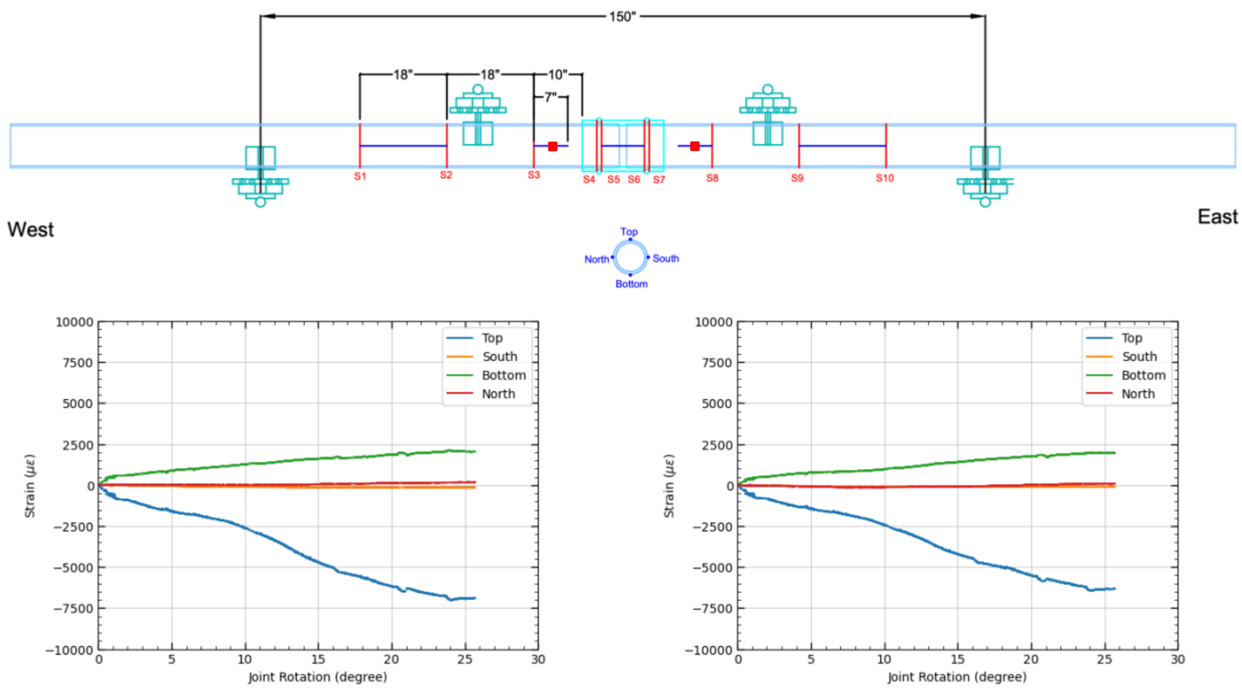

(a) West Pipe **(b) East Pipe**

Figure 4-5 Axial strain vs rotation. (Left) West pipe. (Right) East Pipe.

Figure 4-6 shows the axial strain distribution. In general, consistent with the bending theorem, compressive strain is observed on the top side, whereas tensile strain is captured on the bottom side. The wall is thicker on the fitting compared to the pipes, providing higher stiffness. Consequently, the strains measured on the fitting are generally smaller than those measured on the pipes. Comparing the strain magnitude between the top and bottom sides, one can observe that the magnitude of the strain on the top of the specimen is generally larger than that on the bottom side. This may be due to the pipes rotating within the fitting. The top side of the pipe made better contact with the crown of the fitting, while the gap between the bottom of the pipe and the invert of the fitting became larger, as shown in Figure 4-8. This likely influenced the contact between the gasket, the pipe, and the fitting. Better contact results in more effective force transfer, leading to larger strains on the top side.

Small to zero strains are seen on the springlines (North and South). Examining the north side of the specimen, most sections exhibit almost zero strains; however, compressive strains are found on the first 18 inches of the west pipe. This is because the sensor was not perfectly placed on the springline but was positioned toward the top side, resulting in small compressive strains. On the south side, compressive strains are observed along the entire specimen. As previously mentioned, this is again due to the sensors being installed leaning toward the top side of the pipe.

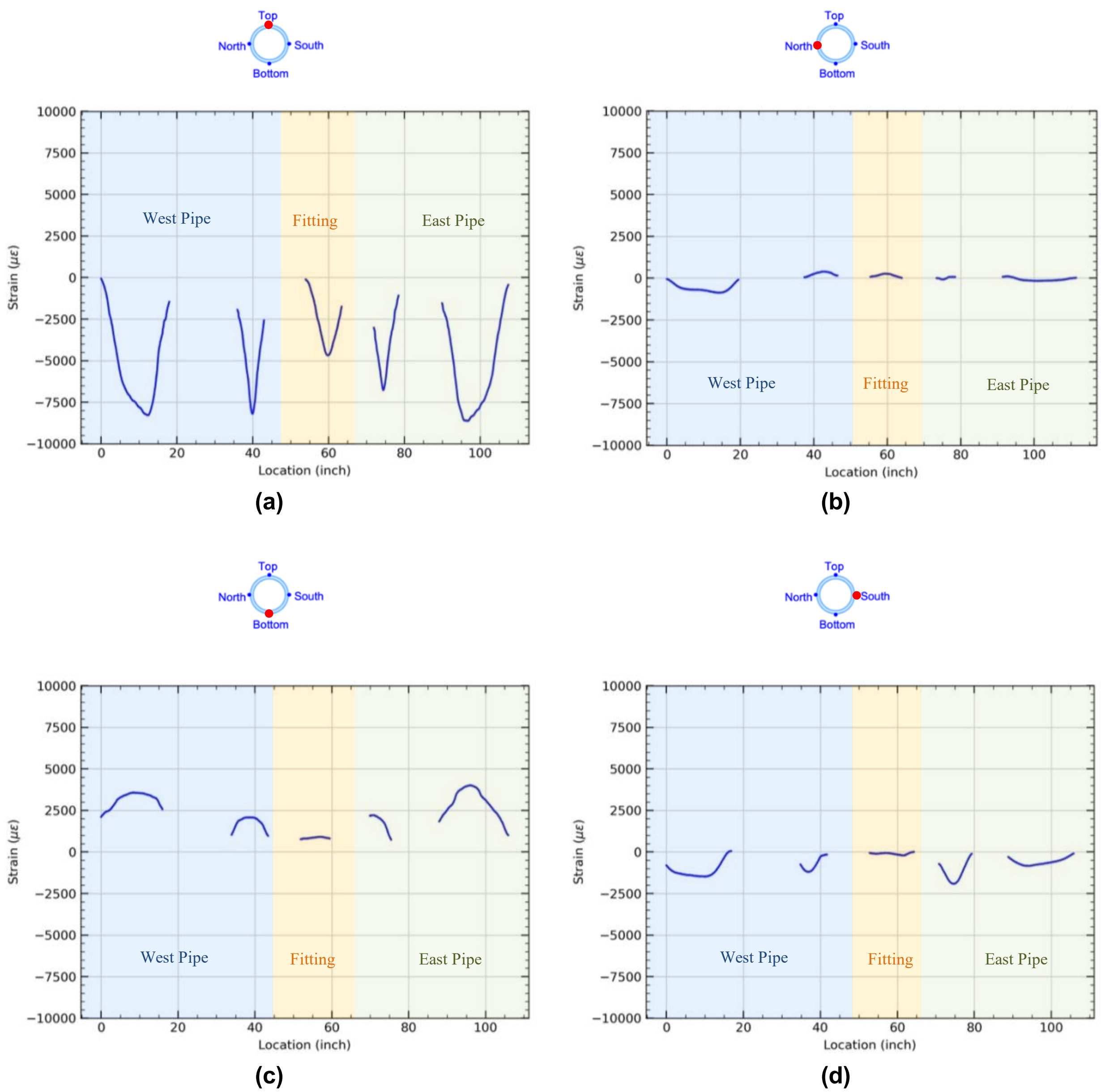

Figure 4-6 Axial strain development of west pipe of under 18-inch joint deflection condition. (a) Top, (b) West side, (c) Bottom, (d) East side

4.5 Hoop Strains

The hoop strain data measured are shown in Figure 4-7. The figure illustrates the results obtained by the sensors positioned on the west pipe (S1-S3), fitting (S4-S7), and east pipe (S8-S10).

The results obtained from S1-S3 and S8-S10 on both pipes show tensile strains on the top and compressive strains on the bottom. This is due to Poisson's effect, where strains in the circumferential direction oppose those in the longitudinal direction with a smaller magnitude. Although the strain distribution patterns are similar, the magnitude of the strain varies. The closer to the fitting, the larger the strain, indicating larger moment.

Examining the sensors located on the outer part of the fitting (S4 and S7), not only is the previously mentioned phenomenon observed (expansion on the top and shrinkage on the bottom), but large tensile strains are also found on the bottom side, as illustrated in Figure 4-8. These additional tensile strains are attributed to the movement of the gasket. As the specimen was pushed down, the bottom side experienced large tensile forces, causing the rubber to move outward. This movement caused the teeth on the rubber to expand the fitting, leading to the tensile strains observed in these specific locations.

For the sensors located in the middle section of the fitting (S5-S6), larger tensile stresses are found on the bottom side. This is due to the pipes pushing the fitting downward, as illustrated in Figure 4-8. As the pipes are pushed down, they rotate within the fitting, causing the bottom of the pipes to contact the invert of the fitting. Consequently, the fitting expands in the circumferential direction on the bottom side.

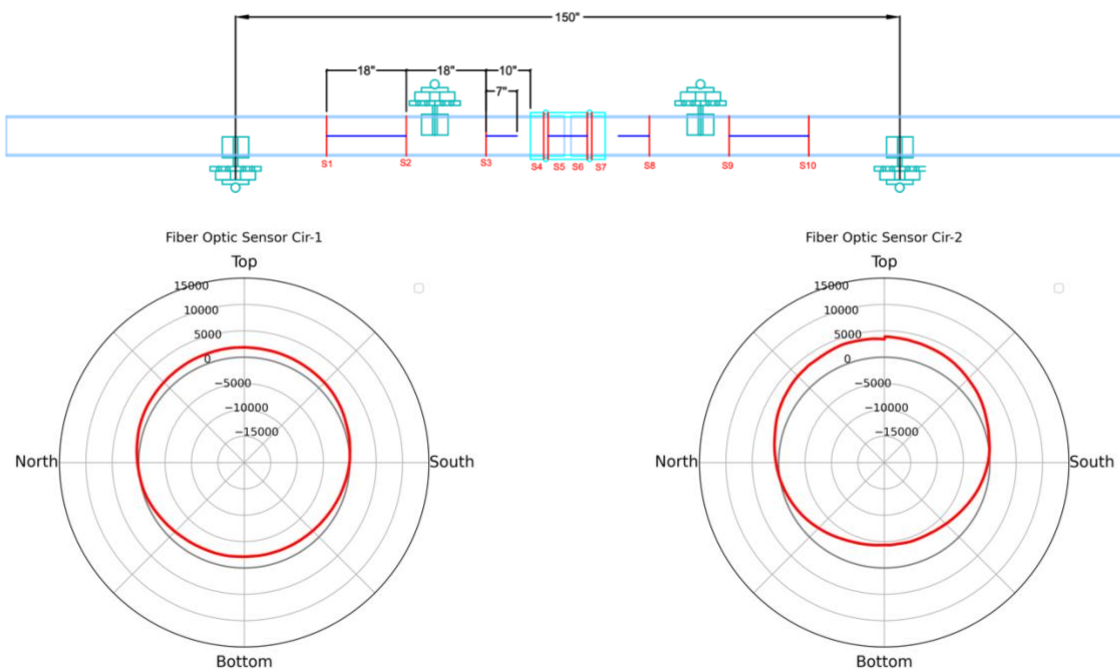

(a) Sensor S1 **(b) Sensor S2**

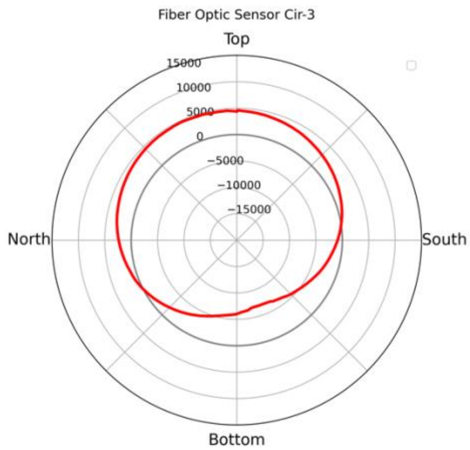

(c) Sensor S3

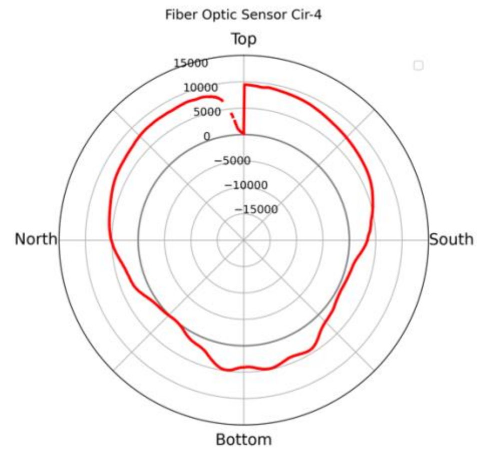

(d) Sensor S4

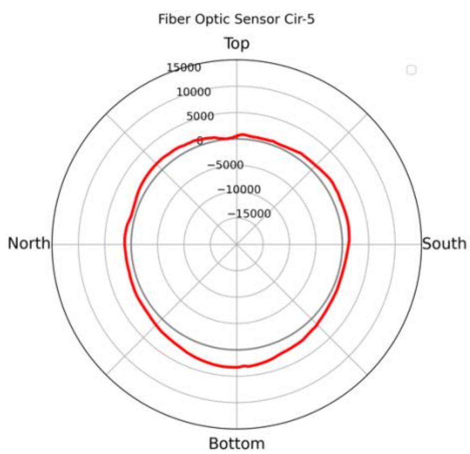

(e) Sensor S5

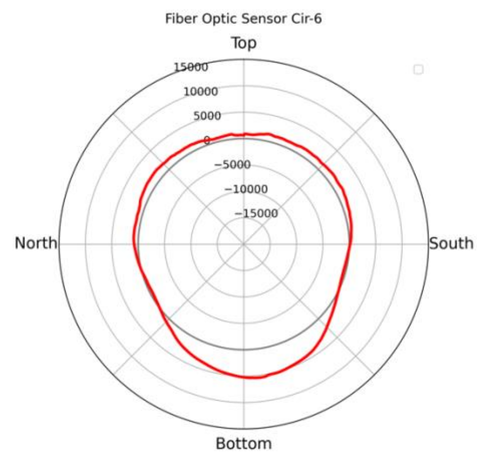

(f) Sensor S6

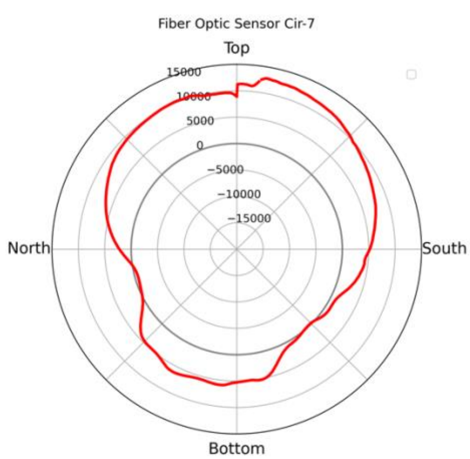

(g) Sensor S7

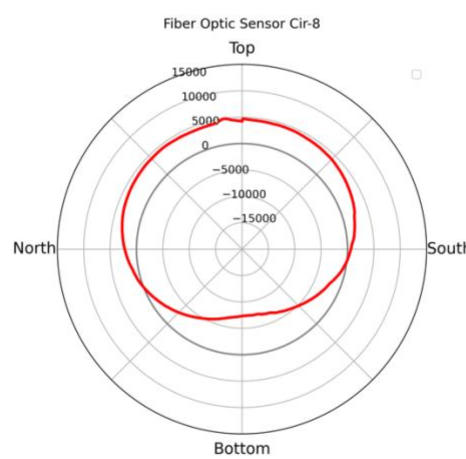

(h) Sensor S8

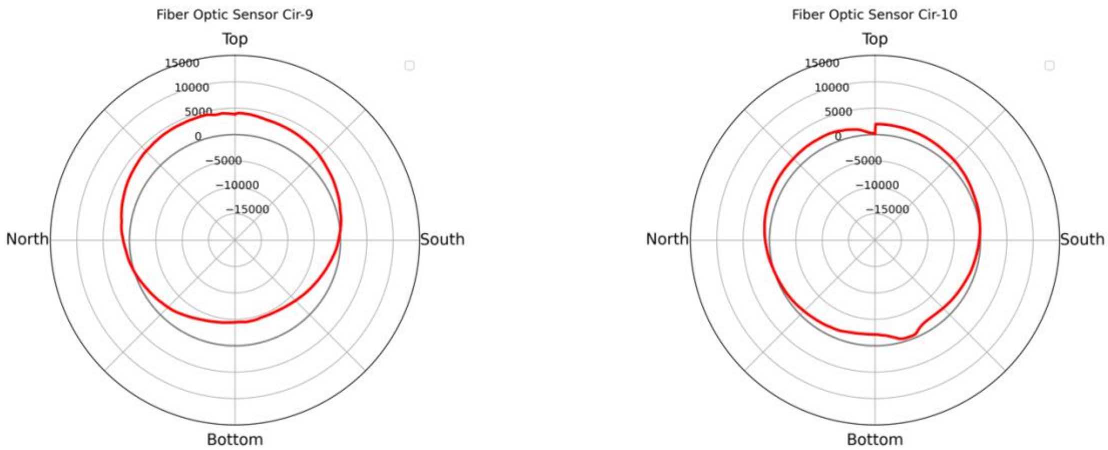

(I) Sensor S9 **(J) Sensor S10**

Figure 4-7 Strain distribution in the circumferential direction under 18-inch joint deflection condition

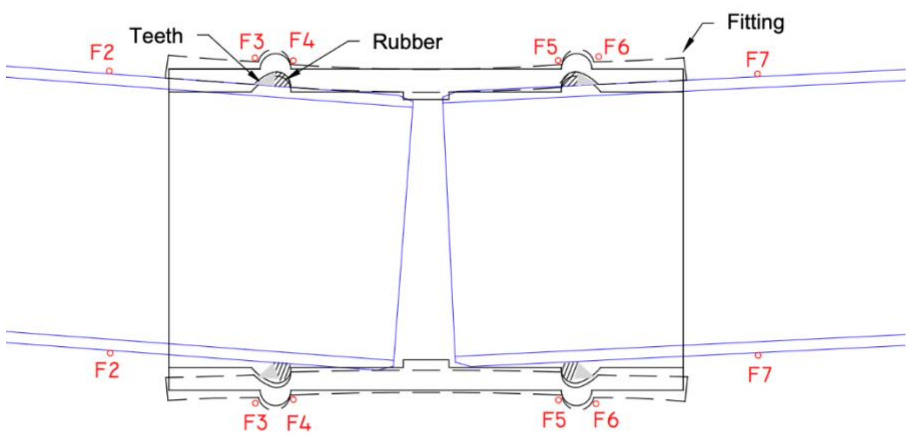

Figure 4-8 Sketch of fitting deformed mechanism

5 Finite Element Analysis

5.1 Overview of Numerical Model

A 3D finite element (FE) analysis of the laboratory four-point bending test was performed using ABAQUS/Standard. The aim of the analysis was to better understand the pipeline behavior under bending by incorporating the complex material nonlinearities and contact interaction of the system components in the analysis.

Figure 5-1 shows the FE model used in this study. The geometry of the pipe and joint model follows the design of the experimental setup. Given the symmetry of the test configuration, only one fourth of the system is modeled, with symmetry boundary conditions in the longitudinal and transverse directions. It consists of four main parts: two iPVC pipe segments, sleeve joint, and the gasket.

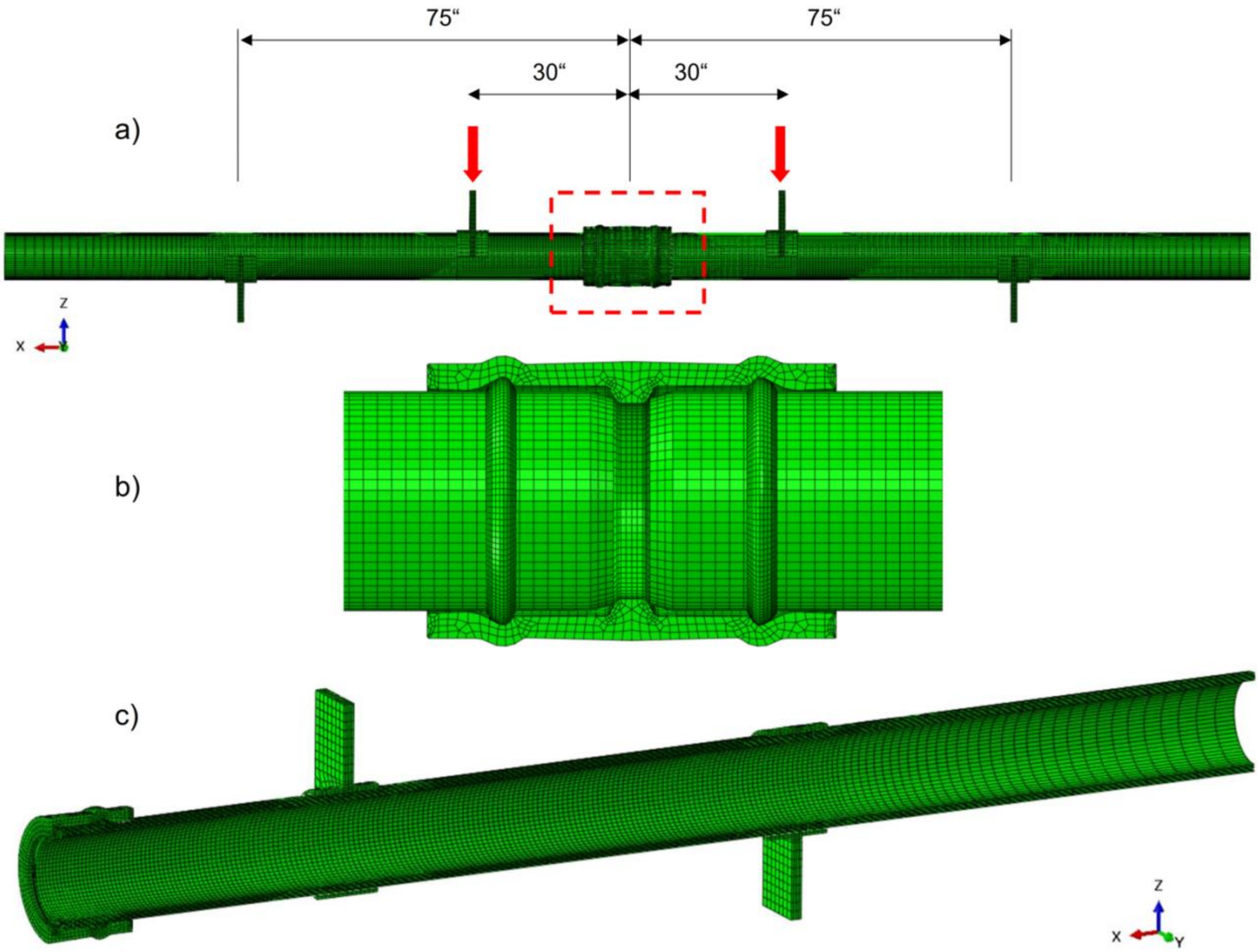

Figure 5-1 3D FE model for the four-point bending test: a) tested iPVC pipe system; b) detail of the joint connection; c) model mesh of one fourth of the system with symmetric boundary conditions in the longitudinal and transverse directions.

The ReiborLok gasket used in the iPVC pipe connection consisted of a circular rubber gasket with multiple steel teeth designed to grip the pipe wall and prevent joint separation. These teeth created local stress concentrations at the contact points, which could initiate failure that might then propagate from these regions.

The mesh sizes of the system components were defined to ensure the accuracy and efficiency of the numerical solution. The interactions among the pipes, the sleeve joint and the gaskets were assumed to be frictional contact, which allowed for finite sliding and separation between the respective interfaces.

A detailed three-dimensional finite element model of the gasket teeth and their interaction with the pipe wall would be difficult and computationally expensive because of complex contact behavior, together with severe geometric and material nonlinearities associated with local indentation, sliding, and progressive damage. Therefore, to reduce computational cost and better understand the overall mechanical behavior of the system, the gasket was modelled as a homogeneous material with equivalent stiffness. The effective gasket stiffness was treated as a parameter in the numerical analysis to investigate its influence on the response of the jointed iPVC pipe system.

The numerical analysis was performed in two consecutive steps: (1) contact between the gasket and the iPVC pipes inserted in the sleeve joint at a distance of 1.5 inch was established; and (2) vertical displacement was applied through two saddles placed at symmetrical points, each 30 inches from the central position of the pipe. The pipe system was supported in the vertical direction by two saddles, each 75" from its central position. The ends of the saddles were free to rotate and slide in the horizontal direction.

To understand the resistance of the gasket stiffness to the pipeline bending response, an additional simulation was performed with a reduced gasket stiffness, highlighting the failure mechanism of the pipeline joint system.

5.2 Determination of Pipe Parameters

The iPVC pipe material characteristics were derived from the tensile coupon test result reported in Price et al. (2018). The pipe material model is defined within the von Mises plasticity theory with isotropic hardening. The engineering stress-strain curve follows a piecewise linear curve measured in the tension coupon test (Figure 5-2). The Young's modulus is Ep = 450 ksi (3.1 GPa), the Poisson's ratio is 0.38, yield strength is 7.6 ksi (52.3 MPa) and peak tensile stress is 7.8 ksi (53.3 MPa) at 5% strain.

The gasket is assumed to be of homogenous elastic material, defined by an effective stiffness EG that is considered as a parameter in the numerical analysis to investigate its influence on the response of the jointed iPVC pipe system.

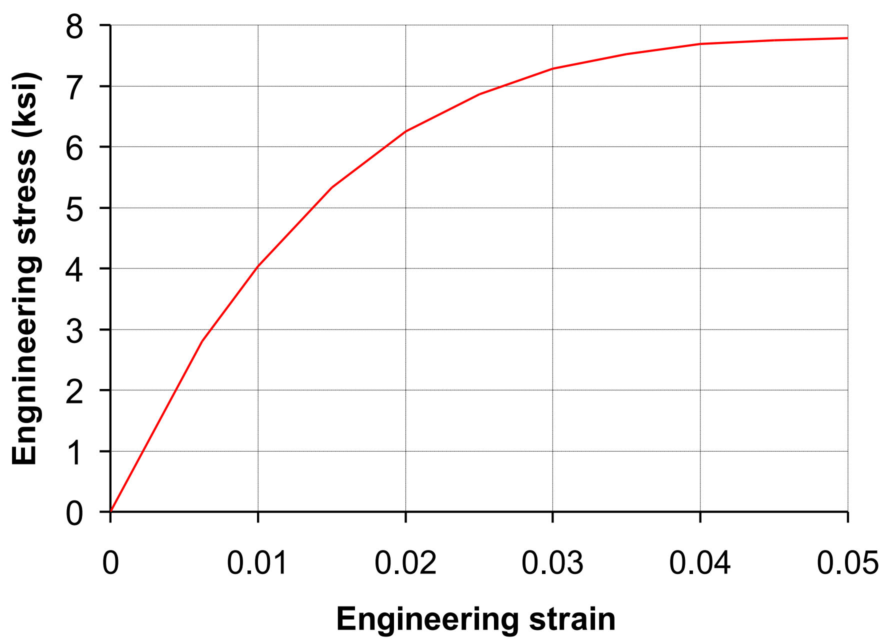

Figure 5-2 Engineering stress-strain curve for the iPVC pipe material.

5.3 Finite Element Analysis Results

This section describes the numerical results of the iPVC pipeline joint simulation of the four-point bending test conducted at CSI. It describes the results considering two significant values of the material stiffness of the gasket: (Case 1) Stiff gasket case: steel material stiffness E_G = 210 GPa; and (Case 2) Soft gasket case: $E_G = 0.01E_p$ = 31 MPa.

Figure 5-3 shows the iPVC pipeline joint response under four-point bending until severe material damage develops in the system. First, the actuator displacement induces vertical movement of the load-transfer beam and the underlying loading saddles, causing rotation of the two pipe segments inside the coupling. This rotation increases the contact pressure of the pipes against the underlying gaskets, as well as contact between the pipe ends and the coupling protrusion, while the pipe crown comes into contact with the upper inner surface (obvert) of the coupling. Consequently, higher local stresses develop in this region for the Case 1 stiffer gasket configuration (Figure 5-3a) compared with the Case 2 softer gasket (Figure 3b).

As the applied actuator displacement increases, the pipe segments continue to rotate, and the pipe ends come into contact with the bottom wall of the fitting. This leads to lower local contact pressure in this region for the stiffer gasket case (Figure 5-3c), which offers greater resistance than the softer gasket case (Figure 5-3d).

The rotating pipe segments and the underlying gaskets continue to press against the coupling wall. In particular, the contact pressure at the upper (obvert) and lower inner surface (invert) of the coupling increase significantly, inducing elevated circumferential deformation and stresses, and making the fitting susceptible to brittle failure (Figure 5-3e and Figure 5-3f).

The case 2 softer gasket configuration is more representative of the initial system response before the gasket locking mechanism engages. The case 1 stiffer gasket configuration is more representative of the response at larger rotations, when the steel locking mechanism increases resistance to joint rotation, leading to greater localized material damage.

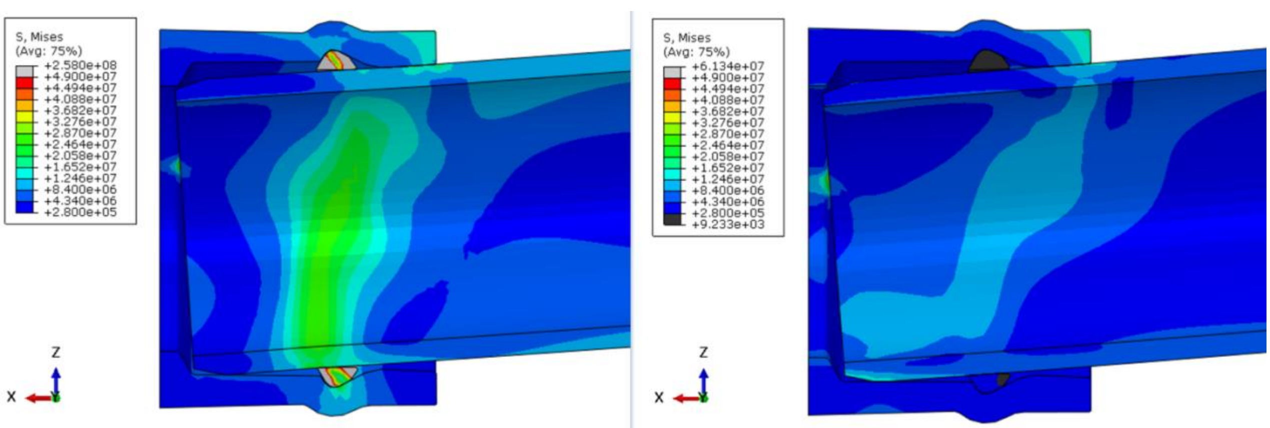

a) b)

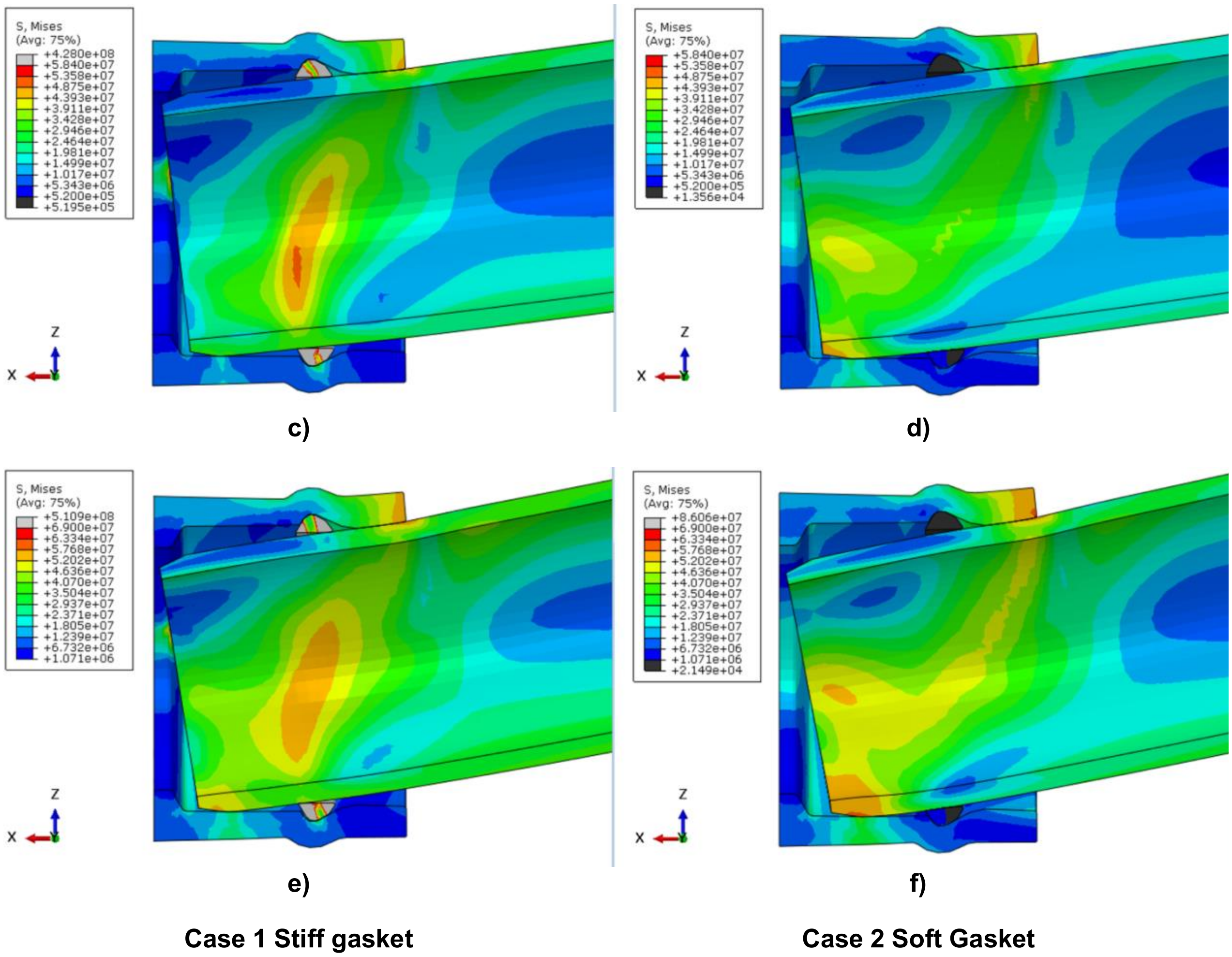

Figure 5-3 iPVC pipeline joint response under four point bending for different values of the joint deflection δ, considering different effective stiffness of gasket material E_G: a) δ = 6 inch, E_G = 210 GPa; b) δ = 6 inch, E_G = 31 MPa; c) δ = 12 inch, E_G = 210 GPa; d) δ = 12 inch, E_G = 31 MPa; e) δ = 18 inch, E_G = 210 GPa; f) δ = 18 inch, E_G = 31 MPa.

The numerical results indicate that the fitting is vulnerable to compression failure, whereas the pipe segments reach excessive tensile deformation at the bottom of the sections bending inside the crown of the fitting. This is consistent with the experimental observations, demonstrating that the fitting failure started on the top side, associated with greater compressive stresses, as shown in Figure 5-4. Pipe failure began at the bottom due to tensile stress, with the shear crack moving upward from the gasket area where stress was highest.

Figure 5-4 Failure of the jointed pipe system, originating at the top of the fitting and bottom of the left sided pipe at the gasket contact interface.

5.4 Comparison of the FE Model and Experimental Data

This section compares the numerical results of the iPVC pipeline joint simulation under four point bending with the strain measurements.

It first analyzes the applied load as a function of the joint deflection, highlighting the main steps characterizing system response. Then, it describes the expected deformation response of pressurized tubular inelastic structures under bending using analytical and numerical solutions. Finally, the obtained pipeline deformation response is compared with the measured distributed strain data using the DFOS for different load levels, giving a better understanding on the pipeline performance.

5.4.1 Force-displacement response of the joint under bending

Figure 5-5 presents the force versus applied displacement curve for the pipeline joint subjected to four-point bending from the FE simulations and experimental test. The analysis results for the pipe system with the stiff steel gasket case (E_G = 210 GPa) are consistent with the experimental curve, with the reaction force increasing monotonically with the applied displacement.

The restraining capacity of the gasket is evident from further comparison with the force-displacement curve resulting from the numerical analysis of the pipe system with the soft gasket case (E_G = 31 MPa) under four point bending test (Figure 5-5). Clearly, the stiffer the gasket material, the greater the applied force necessary to bend the iPVC pipe joint system.

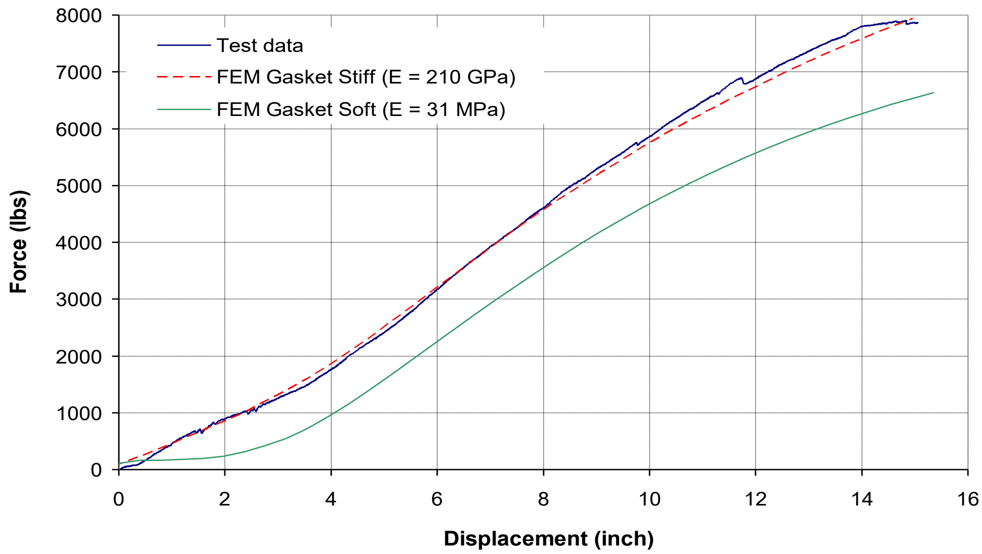

Figure 5-5 Force versus applied displacement during the four point bending test of the iPVC pipe system.

5.4.2 Deformation response in pressurized tubular structures under bending

To better support the finite element analysis of the tested iPVC pipeline system, this section describes the mechanical behavior of pressurized tubular structures under bending, building on the axial strain formulation previously developed in Banushi and Squeglia (2018), which already includes the effects of internal pressure and nonlinear isotropic material behavior within the framework of von Mises plasticity theory. The present work extends that formulation to derive the corresponding hoop strains in addition to the axial strains.

The hoop strain results from the combined effect of internal pressure and bending. While internal pressure induces circumferential tensile strain, bending generates longitudinal compressive and tensile strains at the top and bottom of the tubular structure, respectively. Through the Poisson effect, these longitudinal strains produce associated tensile and compressive hoop strains at the top and bottom, respectively. In addition to this beam-like bending response, the tubular cross-section tends to ovalize, introducing further circumferential deformation and additional tensile hoop strains at both top and bottom of the section.

Figure 5-6 shows the hoop strain response as a function of the longitudinal (axial) strain in tubular structures under bending for different levels of internal pressure, comparing the developed analytical solution with the 3D continuum model results. Clearly, the magnitude of the hoop strains increases with increasing axial strains. This comparison provides a useful framework for interpreting the distributed strain measurements in the longitudinal and circumferential directions presented in the following section.

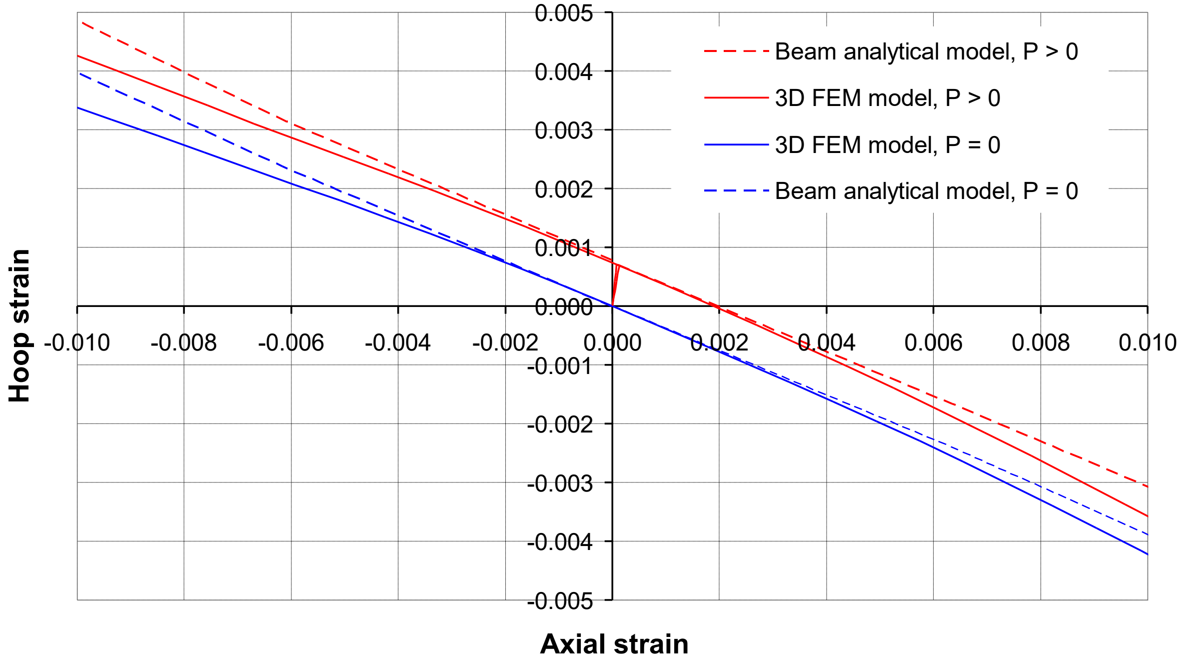

Figure 5-6 Hoop strain response as a function of the longitudinal (axial) strain in pressurized tubular structures under bending, considering the effect of material nonlinearities within the von Mises plasticity theory.

5.4.3 Strain response of the pipe system in the longitudinal direction

Figure 5-7 and Figure 5-8 show the longitudinal strain distribution in the pipeline obtained from the test measurements and the numerical simulation for increasing levels of joint deflection, for the stiff gasket case (EG = 210 GPa) and the soft gasket case (EG = 31 MPa), respectively.

The coupling and the connected pipeline segments show different strain responses under bending, representative of thick short and long tubular structures, respectively. For small joint deflection levels (6 inch), the measured strains at the top and bottom of the pipe segments are of the same order of magnitude, as shown in Figure 5-7a. As the joint deflection increases, the measured strains at the pipe crown become approximately twice those at the invert. The DFOS measurements between the supports and loading points at the pipe crown also show a linear variation along the pipe axis, consistent with the bending moment increasing linearly with the distance from each support point.

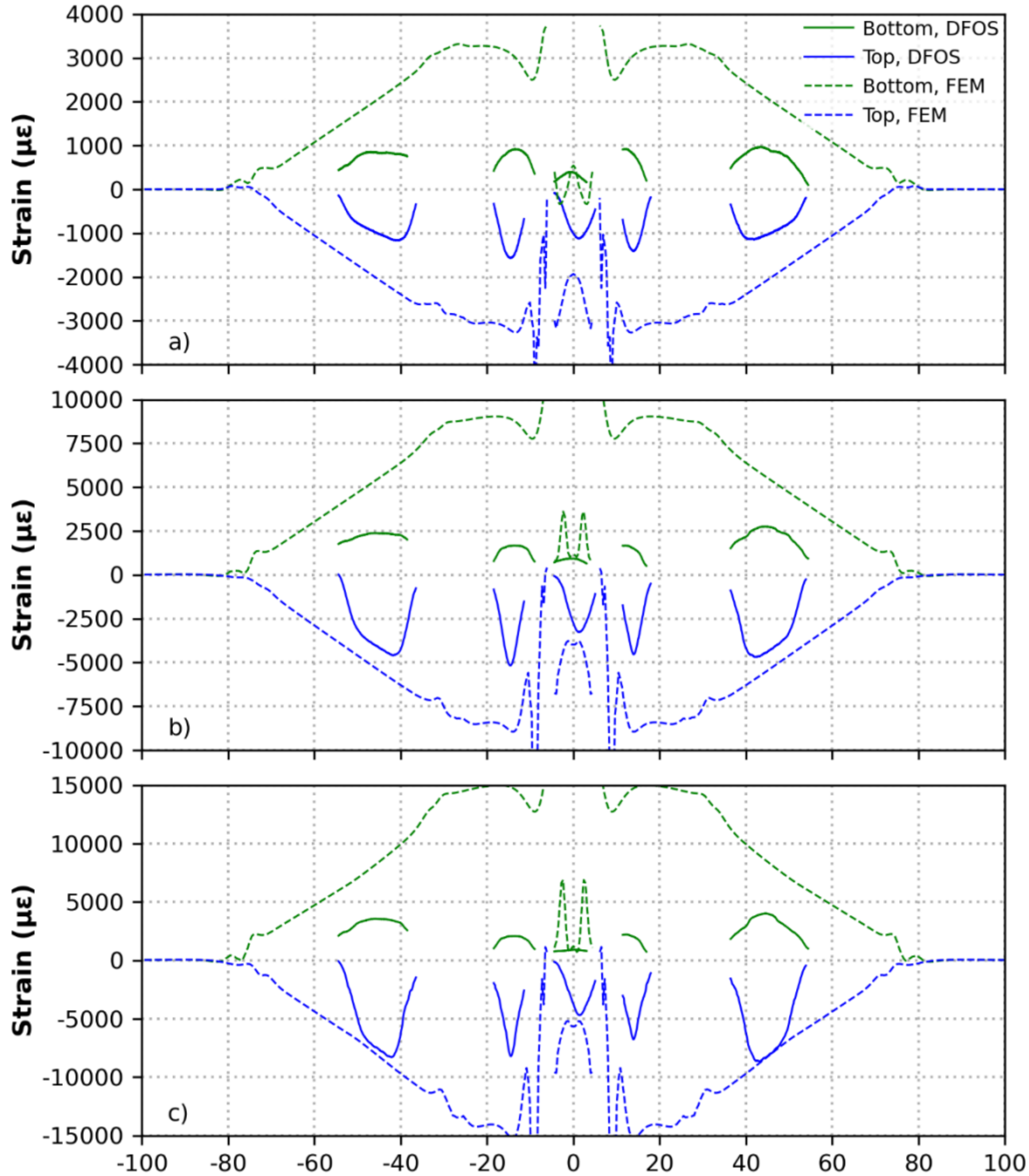

Figure 5-7 Longitudinal strain distribution in the pipeline system according to the test measurements and numerical simulation with the stiff gasket case (E_G = 210 GPa) at an amount of joint deflection equal to: a) 6 inch; b) 12 inch; c) 18 inch.

Conversely, the magnitudes of the longitudinal strains at the top of the coupling exceed those at the bottom by more than a factor of two throughout the bending test, reflecting the distinct structural behavior of the coupling compared to the longer pipe segments it connects.

The numerical model with the softer gasket case more accurately predicts the measured pipeline strain response at small (6 inch) and moderate (12 inch) joint deflections, as shown in Figure 5-8a and Figure 5-8b respectively. Conversely, at larger joint deflections (18 inch), the model with the stiffer gasket case better matches the measured strain response, as shown in Figure 5-7c.

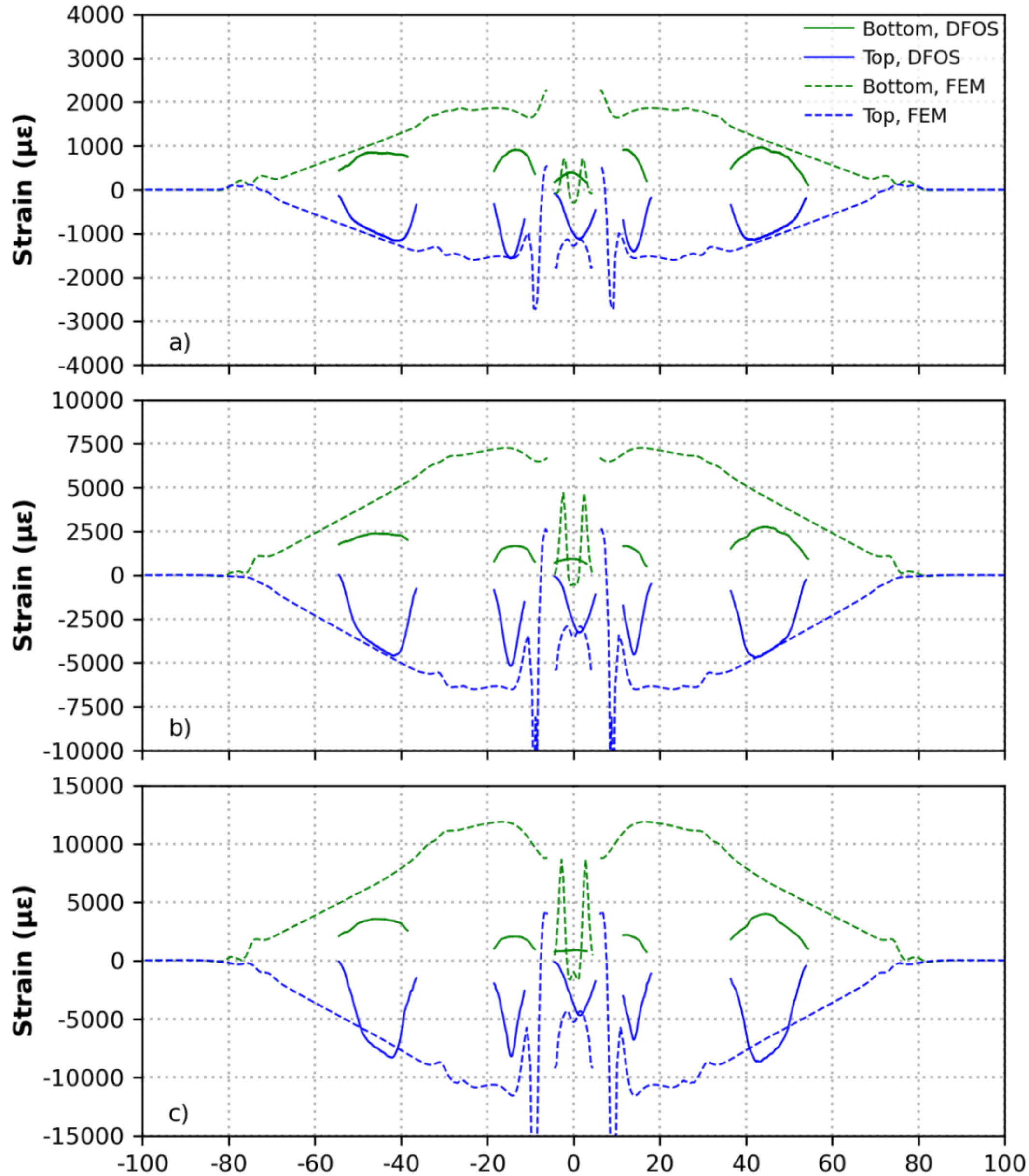

Figure 5-8 Longitudinal strain distribution in the pipeline system according to the test measurements and numerical simulation with the soft gasket case (EG = 31 MPa) at an amount of joint deflection equal to: a) 6 inch; b) 12 inch; c)18 inch.

5.4.4 Strain response of the pipe system in the circumferential direction

The coupling and the connected pipeline segments show a different hoop strain response under bending, representative of thick short and long tubular structures, respectively.

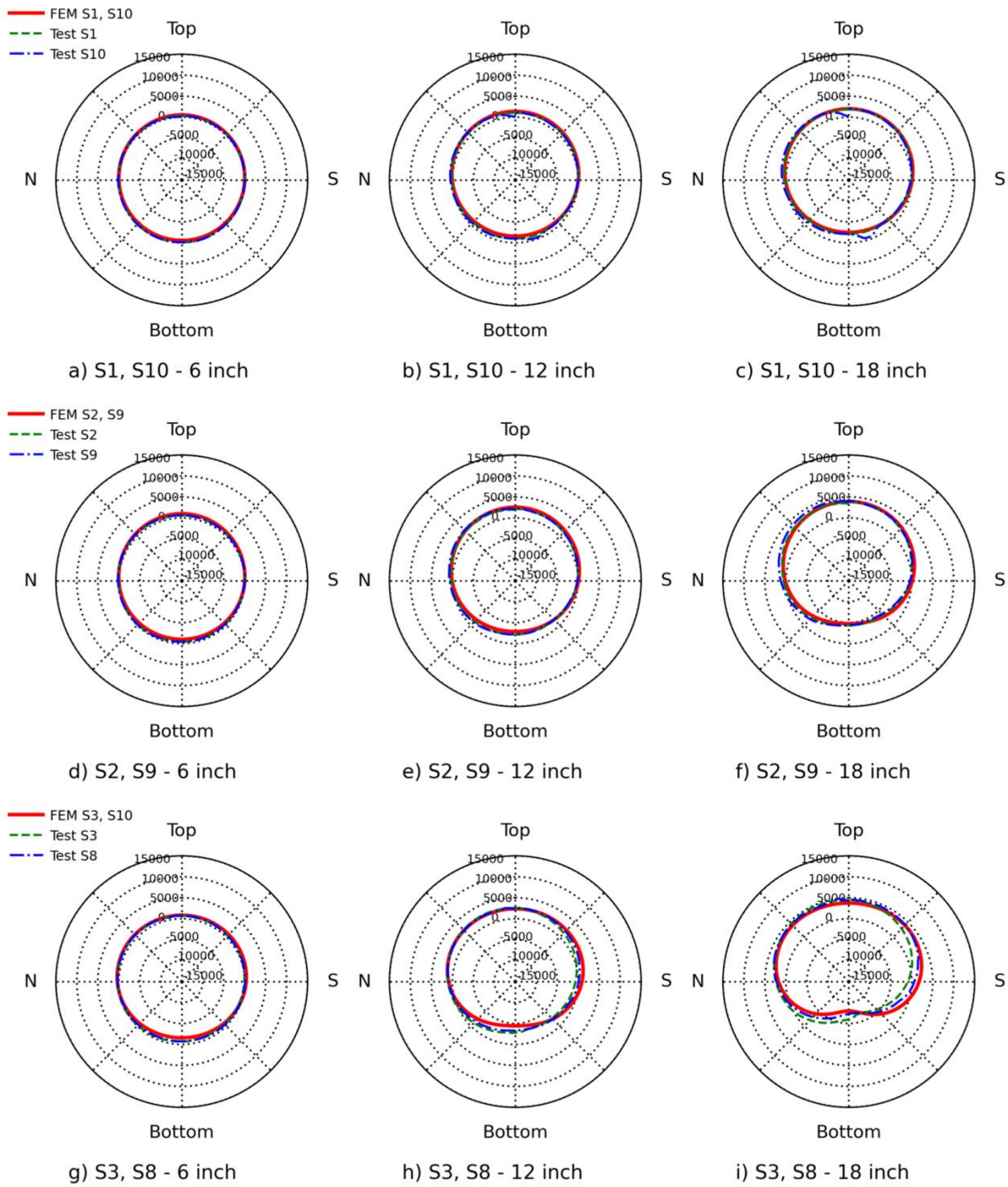

Figure 5-9 Circumferential strain distribution in the pipeline segments according to the test measurements and numerical simulation with stiff gasket (E_G = 210 GPa) for joint deflections of 6, 12, and 18 inch: (a)–(c) sensors S1 and S10; (d)–(f) sensors S2 and S9; and (g)–(i) sensors S3 and S8. :

Figure 5-9 and Figure 5-10 show the circumferential strain distribution in the pipeline segments obtained from the test measurements and the numerical simulation for increasing levels of joint deflection, for the stiff gasket case (E_G = 210 GPa) and the soft gasket case (E_G = 31 MPa), respectively. The measured hoop stains in the pipe segments increase towards the system centerline, reflecting the variation of the bending moment along the pipeline axis. This is consistent with the hoop strain results obtained from the finite elements simulations, as shown in Figure 5-9 and Figure 5-10.

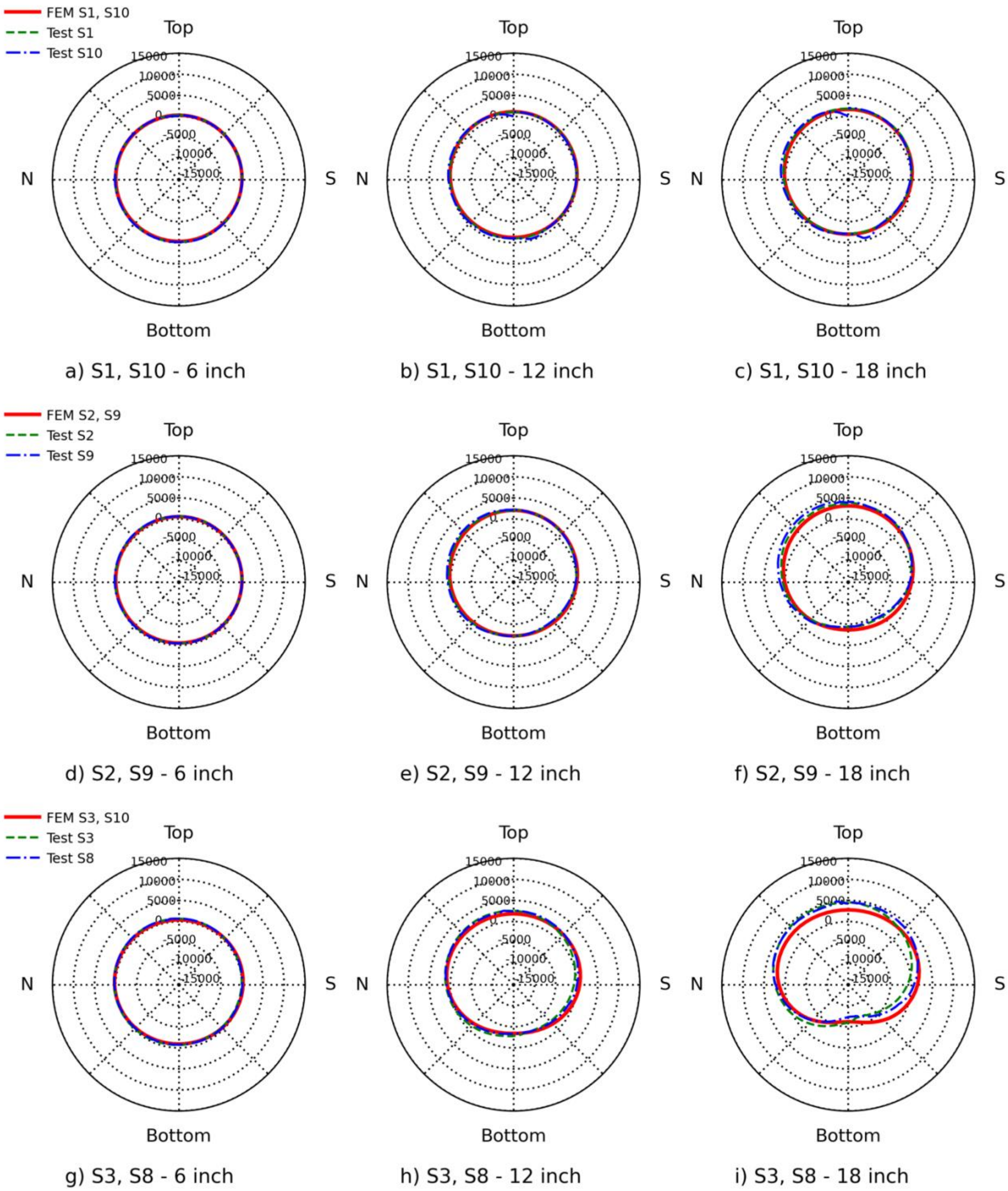

Figure 5-10 Circumferential strain distribution in the pipeline system according to the test measurements and numerical simulation with soft gasket (E_G = 31 MPa) for joint deflections of 6, 12, and 18 inch: (a)–(c) sensors S1 and S10; (d)–(f) sensors S2 and S9; and (g)–(i) sensors S3 and S8.

Figure 5-11 and Figure 5-12 show the circumferential strain distribution in the coupling obtained from the test measurements and the numerical simulation for increasing levels of joint deflection, for the stiff gasket case (EG = 210 GPa) and the soft gasket case (EG = 31 MPa), respectively. The hoop strains measured in the coupling by the sensors located closer to the centerline (S5 and S6) are lower than those recorded by the sensors nearer to its ends (S4 and S7), because of the greater contact pressure exerted close to the centerline by the rotating pipe segments. The hoop strains measured in the coupling by the outer sensors (S4 and S7) are greater at the top, exceeding 1% at 18 inch of joint deflection, whereas those measured by the inner sensors (S5 and S6) are greater at the bottom, due to the pressure exerted by the pipe end sections against the underlying gasket and the coupling invert.

The numerical model with the softer gasket case more accurately predicts the measured circumferential strain response at small (6 inch) and moderate (12 inch) joint deflections, both in the pipeline segments (Figure 5-10a and b) and in the sleeve joint region (Figure 5-12a and b).

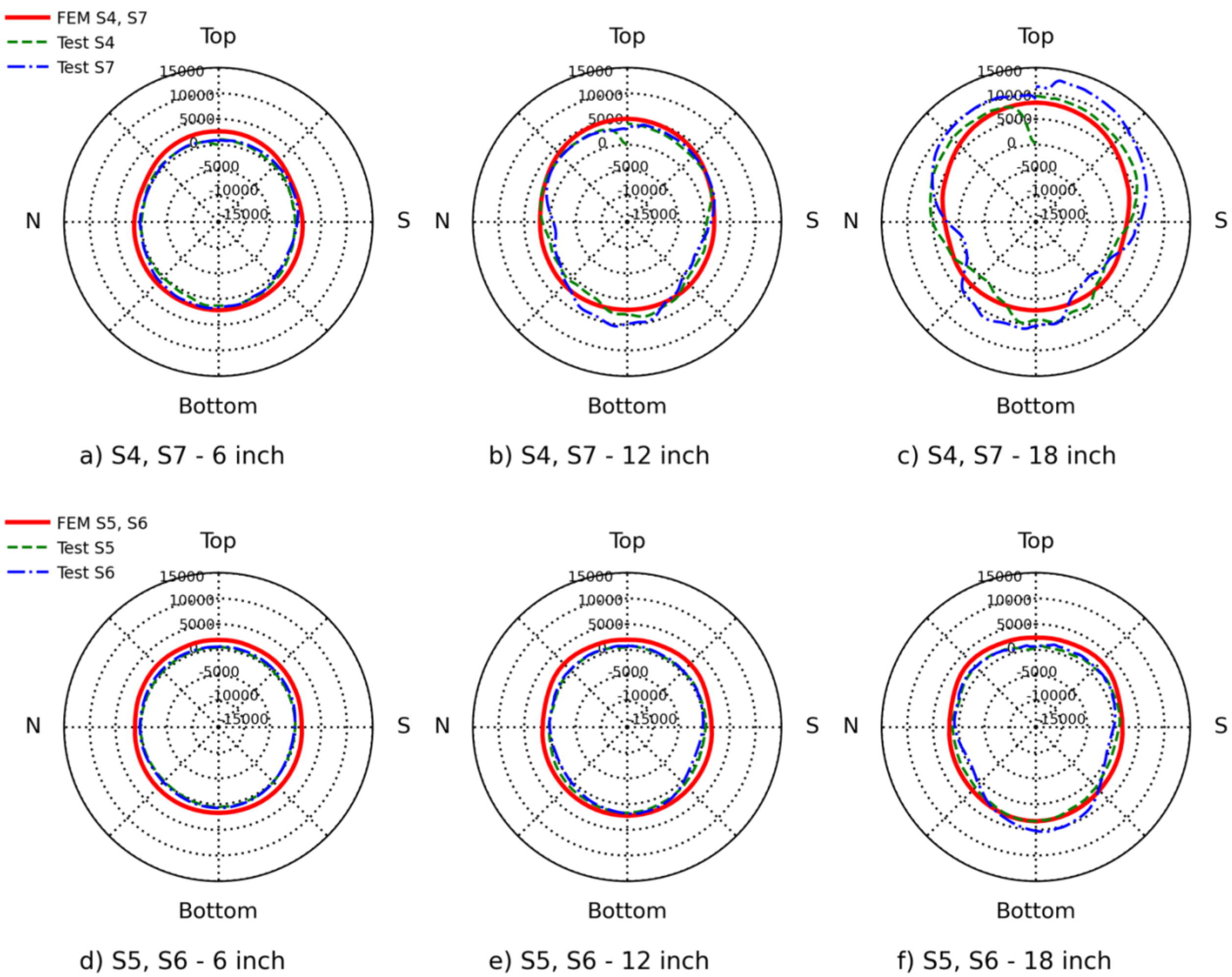

Figure 5-11 Circumferential strain distribution in coupling according to the test measurements and numerical simulation with stiff gasket (E_G = 210 GPa) for joint deflections of 6, 12, and 18 inch: (a)–(c) sensors S4 and S7; (d)–(f) sensors S5 and S6.

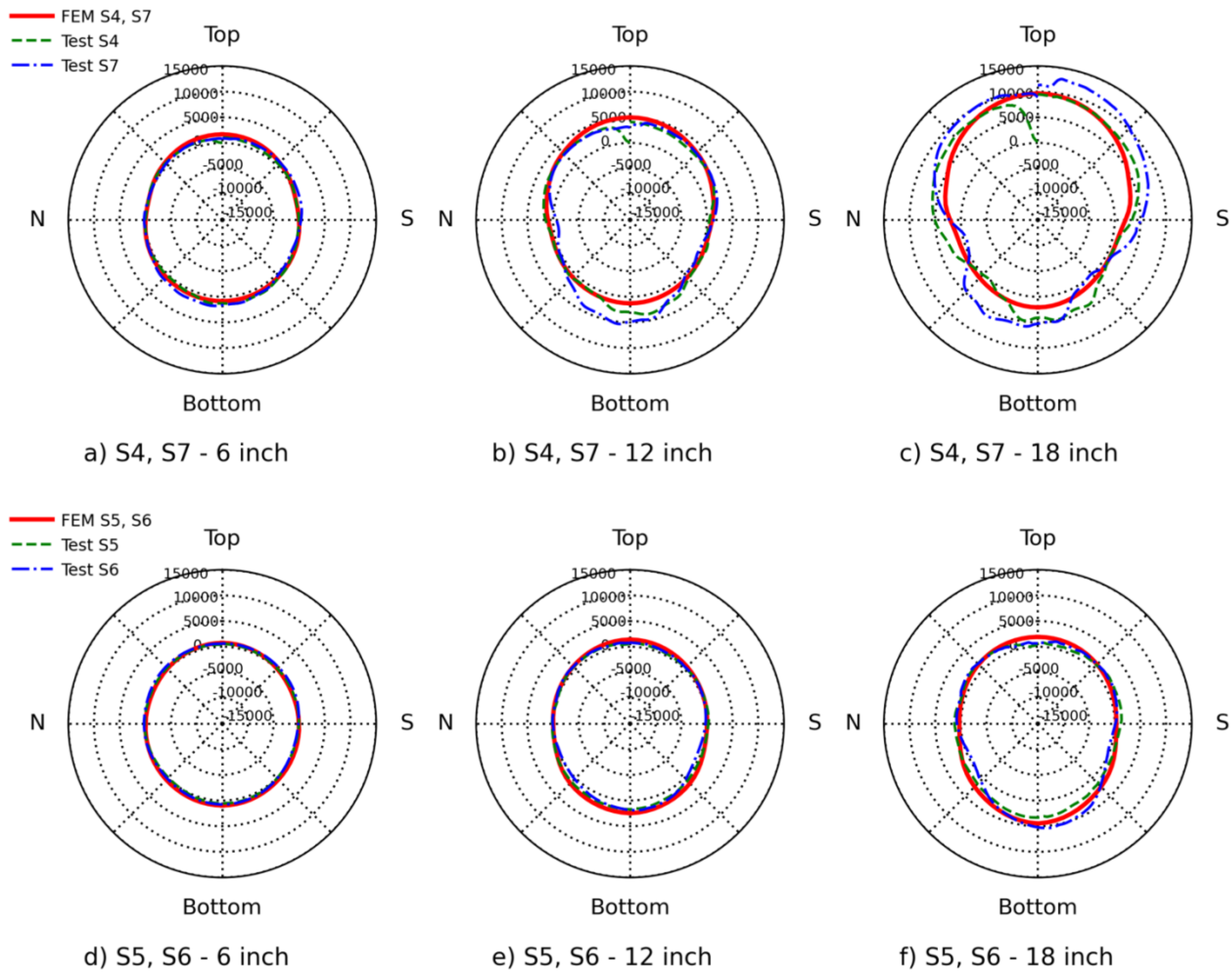

Figure 5-12 Circumferential strain distribution in the coupling according to the test measurements and numerical simulation with soft gasket (E_G = 31 MPa) for joint deflections of 6, 12, and 18 inch: (a)–(c) sensors S4 and S7; (d)–(f) sensors S5 and S6.

6 Conclusions

This report outlines the findings of the four-point bending experiments conducted on 8-inch AWWA C900 DR14 iPVC pipes fitted with ReiberLok rubber gaskets under bending force. The objective was to test the pipes until severe damage or water leakage occurred.

Failures in both the pipe and the fitting initiated near the ReiberLok gasket due to local stress concentrations from the gasket's teeth. The fitting failure began on the top side, where the compressive force was greatest, and propagated due to shear forces along the sides to the bottom. Conversely, the west pipe failure started on the bottom side due to tensile stress, with the shear crack propagating upwards, originating near the gasket where stress concentration was highest.

Two approaches for computing rotations were utilized: the VWP approach and the HWP approach. The results from both methods closely aligned, showing maximum joint rotations of 28.07 degrees and 26.38 degrees, respectively, with a maximum moment of 177.76 kip-in.

Axial strain measurements obtained from the DFOS sensors confirmed that the pipe response is consistent with classical bending theory: compressive strains were observed on the top side, tensile strains on the bottom, and minimal stress on the springlines. The pipes were expanding in the cirumferetial direction on the top side and compressing on the bottome side. This is due to Poison's effect. Large tensile hoop strains on the bottom side are found on the outer side of the fitting, which is due to gasket movement. As the specimen bent, tensile forces caused the rubber to move outward, expanding the fitting and resulting in observed tensile strains. Sensors in the middle section of the fitting (S5-S6) also recorded tensile stresses on the bottom side. This was due to the downward movement and rotation of the pipes within the fitting, causing circumferential expansion of the fitting at the bottom. DFOS dataset not only helps to understand the deformation and failure mechanism of the pipe, but also provides a valuable basis for validating the subsequent numerical model analysis.

Two gasket stiffnesses were modeled in the finite element analysis to represent different stages of gasket behavior: an early stage and a near-failure stage. In the early stage, the metal teeth have not yet fully engaged with the pipe, so a softer gasket provides a more realistic representation. As the pipe undergoes bending, however, the teeth progressively bite into the pipe, and the gasket behavior becomes better approximated by the stiffer model. The numerical results indicate that the fitting is particularly susceptible to compressive failure. At the same time, the pipe segments experience significant tensile deformation near the gaskets and at the bottom of the beveled sections, as well as bending within the crown of the fitting. These findings are consistent with experimental observations: failure of the fitting initiates at the top side, where compressive stresses are highest, while pipe failure begins at the bottom due to excessive tensile stresses. A shear crack then propagates upward from the vicinity of the gasket, driven by elevated stress concentrations.

7 References

Banushi, G., Squeglia, N. (2018). Seismic analysis of a buried operating steel pipeline with emphasis on the equivalent-boundary conditions. Journal of Pipeline Systems Engineering and Practice, 9(3), 04018005.

PPI Pipe (n.d.). iPVC Water Pipe. https://ipvcpipe.com/eng/sub/ipvc01.php

Price, D., Berger, B. A., O'Rourke, T. D., Stewart, H. E., Wham, B. P., Pariya-Ekkasut, C., Hall, H. (2018). Performance Evaluation of iPVC Pipe under Earthquake-Induced Ground deformation. School of Civil and Envr. Engr., Cornell University, April, < https://lifelines. cee. cornell. edu> (Dec. 4, 2020).

Wu, J., Jiang, H., Su, J., Shi, B., Jiang, Y., & Gu, K. (2015). Application of distributed fiber optic sensing technique in land subsidence monitoring. Journal of Civil Structural Health Monitoring, 5(5), 587-597.

Appendix A: Distributed Fiber Optic Sensing

Using the physical properties of light, fiber-optic sensing can detect changes in temperature, strain, and other parameters when light travels along a fiber, which uses fiber-optic cables as sensors and can measure over long distances at 100 to 1000s of points on a single cable or multiplexed cables depending on the analyzer used. Compared to the other sensing technologies, fiber-optic sensing has distinct advantages such as small size, light weight, and strong resistance to corrosion and water. Distributed fiber optic sensing consists of two main components, an analyzer, and fiber-optic cables. LUNA ODiSI 6000 series integrator was used as the analyzer, and NanZee Sensing Technology Co manufactured the fiber-optic cables in the experiments.

LUNA Interrogator

Figure A-1. LUNA ODiSI 6000 Series optical distributed sensor interrogator (LUNA, 2022)

LUNA ODiSI 6104 is an optical distributed sensor interrogator that can provide thousands of strain or temperature measurements per meter of a single high-definition fiber sensor. High-Definition H.D.D) Sensors - Strain & Temperature (HD-SC) temperature sensors utilize an advanced interrogation mode of the ODiSI to increase the accuracy of measurements when the sensors are subjected to strain, such as in embedded and surface-mount installations. It can achieve a sensor gauge pitch (the distance between two measurement points) as small as 0.65 mm, a sensor length of up to 100 m, and a measurement rate of up to 250 Hz with an accuracy of less than ±1 microstrain.

Fiber-optic Cable

Two types of fiber optic cables manufactured by NanZee Sensing Technology Co. were used; (a) 5 mm diameter armored cable (NanZee 5mm) and (b) 0.9 mm diameter cable (NanZee 0.9mm). Table A-1 lists the information on the cables. The difference between the two cables is the thickness and material of the coating. NanZee, a 5mm cable, provides a sheath layer and steel reinforcement, resulting in better protection to the optical core; hence, it can be used for the actual field application. The coating of NanZee 0.9mm cable is thinner than NanZee 5mm cable. NanZee 0.9mm cable has less protection, but a more sensitive strain response is achieved.

Table A-1 Schematic illustration of the selected strain sensor cable (Wu et al., 2015)

Brand	NanZee Sensing Technology Co.	NanZee Sensing Technology Co.
Model	NZS-DSS-C07	NZS-DSS-C02
Cross section	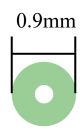	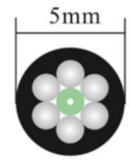
Side view